CHALMERS
UNIVERSITY OF TECHNOLOGY

Near-Field RIS-Aided Localization Under Deliberate Model Misspecification: Bounds and Algorithms

Citation for the original published paper (version of record):
Sun, B., Keskin, M., Pourafzal, A. et al (2026). Near-Field RIS-Aided Localization Under Deliberate Model Misspecification: Bounds and Algorithms. IEEE Transactions on Wireless Communications, 25: 13945-13961. http://dx.doi.org/10.1109/TWC.2026.3672291

Near-Field RIS-Aided Localization Under Deliberate Model Misspecification: Bounds and Algorithms

Bo Sun, *Member, IEEE*, Musa Furkan Keskin, *Member, IEEE*, Alireza Pourafzal, *Member, IEEE*, Hui Chen, *Member, IEEE*, Moustafa Rahal, Jukka Talvitie, *Member, IEEE*, Henk Wymeersch, *Fellow, IEEE*, and Mikko Valkama, *Fellow, IEEE*

***Abstract*—This paper investigates the optimization of reconfigurable intelligent surfaces (RIS) for near-field user equipment (UE) localization in the presence of channel spatial non-stationarity (SNS) across elements and the involved deliberate model misspecification. Traditional far-field localization techniques struggle to maintain accuracy in near-field scenarios characterized by spherical wavefronts (SWFs) while algorithms relying on a full-fledged near-field model with SNS and SWF necessitate long transmission durations to estimate a large number of parameters. To address these challenges, we propose a novel low-complexity localization algorithm based on a misspecified model that reduces the number of unknown channel parameters with limited impact on accuracy. A misspecified Cramér-Rao bound (MCRB) analysis is also performed to evaluate theoretical performance degradation due to the involved model misspecification. Additionally, we propose a codebook design that leverages coarse UE location information to enhance localization accuracy. Numerical simulations validate the effectiveness of the proposed estimation method and highlight the advantages of using the proposed codebook.**

***Index Terms*—Reconfigurable intelligent surfaces (RIS), near-field localization, codebook optimization, channel non-stationarity, misspecified Cramér-Rao bound (MCRB).**

I. Introduction

THE wireless communication and sensing technologies for beyond fifth generation (B5G) and sixth-generation (6G) networks are in an active research and development phase to meet the increasing demands for ultra-reliable connectivity, high data rates and precise localization [1]. Reconfigurable intelligent surface (RIS) have attracted attention for their ability to manipulate the signal propagation environment. Such RISs are generally composed of numerous programmable elements, which can reflect, refract, and even absorb electromagnetic waves to optimize signal quality [2], [3]. Due to the lack of RF chains, passive RIS can be considered more economical for addressing critical challenges, including signal blockage and power inefficiencies, which are particularly prominent with higher frequency bands like millimeter-wave and terahertz (THz), compared to multi-antenna and relay based solutions [4], [5]. Moreover, the integration of RIS into the cellular localization task and related signal processing solutions introduces more degrees of freedom and enhances the accuracy by constructing intelligent radio environments [6], [7].

Early works on RIS-based systems focused primarily on phase-only control to steer reflections [8]. Recent research has expanded toward architectures capable of manipulating both phase and amplitude. For example, simultaneous transmitting and reflecting (STAR) RISs enables simultaneous reflection and transmission, extending coverage to both sides of the surface [9], [10]. In addition, practical RIS prototypes already exhibit non-unit reflection amplitudes, partial absorption, and tunable complex coefficients [11], [12]. These findings motivate amplitude-aware surface models, such as absorptive reconfigurable intelligent surfaces (ARISs) [13], [14], [15], which intentionally dissipate part of the incident energy. ARISs have demonstrated benefits, e.g., in interference mitigation [13], physical-layer security [14], and frequency-selective filtering [15]. Importantly, unlike ideal reflective designs, both STAR RISs and ARISs permit non-unit reflection magnitudes, providing additional flexibility for beamforming and codebook design [16].

Most existing *RIS-aided localization works* rely on far-field propagation models, exploiting angle-of-arrival (AoA), received signal strength (RSS), time-of-arrival (ToA), or time-difference-of-arrival (TDoA) measurements under planar wave assumptions [17], [18]. For example, monostatic sensing with single- and double-bounce separation [19], joint sensing and communication related beam optimization [20], as well as environment mapping using RIS-assisted paths [21] have been investigated. While often computationally efficient, far-field models become inaccurate for very large arrays or

Received 6 June 2025; revised 27 November 2025; accepted 5 March 2026. Date of publication 17 March 2026; date of current version 20 March 2026. This work was supported in part by HORIZON-MSCA through Project SMALL-6G under Grant 101201808; in part by Business Finland through the 6G-ISAC Project; in part by the Smart Networks and Services Joint Undertaking (SNS JU) Project 6G-DISAC through the EU's Horizon Europe Research and Innovation Program under Grant 101139130; in part by Swedish Research Council (VR) under Grant 2022-03007 and Grant 2024-04390; in part by the Research Council of Finland under Grant 352754, Grant 357730, and Grant 359095; and in part by China Scholarship Council under Grant 202107960017. An earlier version of this paper was presented at the 2024 IEEE SPAWC [DOI: 10.1109/SPAWC60668.2024.10694423]. The associate editor coordinating the review of this article and approving it for publication was A. Guerra. *(Corresponding author: Mikko Valkama.)*

Bo Sun, Jukka Talvitie, and Mikko Valkama are with Tampere University, 33720 Tampere, Finland (e-mail: mikko.valkama@tuni.fi).

Musa Furkan Keskin, Alireza Pourafzal, and Henk Wymeersch are with the Chalmers University of Technology, 412 96 Gothenburg, Sweden.

Hui Chen is with the Chalmers University of Technology, 412 96 Gothenburg, Sweden, and also with the Department of Electronic and Electrical Engineering, University College London, WC1E 7JE London, U.K.

Moustafa Rahal is with Vicinity Technologies Ltd., BS1 3AG Bristol, U.K.

Digital Object Identifier 10.1109/TWC.2026.3672291

high-frequency bands where the near-field region expands significantly [22]. Recent electromagnetic analyses demonstrate that even simplified near-field approximations may lead to substantial localization bias [23], while mutual-coupling-aware studies confirm the presence of hardware-induced distortions in realistic deployments [24]. On the other hand, and very importantly, spherical wavefront (SWF) behavior in the near field enables direct range estimation even in narrowband systems, offering accuracy improvements over far-field setups and models [25], [26], [27], [28], [29].

Motivated by these advantages, many researches have addressed *RIS-aided near-field localization* [18], [30], [31], [32], [33], [34], [35], [36], [37]. To this end, RSS-based solutions offer simplicity but lower accuracy compared to approaches exploiting ToA/AoA [18], [30]. Refined channel models have been proposed to decouple distance and angle estimation [31], while segmentation of large RIS panels into smaller sub-RIS regions enables localization under far-field approximations [32]. Codebook optimization has also been explored to improve near-field accuracy, either by steering beams toward coarse user locations [33] or by minimizing Cramér-Rao bound (CRB)-based metrics using spatially-focused or derivative beams [34], [35]. However, all these works assume ideal RIS amplitude responses, neglecting practical amplitude variations arising from hardware impairments or propagation non-stationarity, while often also calling for extensive amounts of pilot or reference symbols. As shown in [38], simplified models may introduce systematic bias, making mismatch-aware analysis essential. The misspecified Cramér–Rao bound (MCRB) framework was recently applied in [36] to analyze phase-dependent amplitude variations, while our preliminary work in [37] proposed a misspecified model to reduce the number of amplitude parameters in non-stationary RIS channels.

Building on these advancements, this article addresses critical challenges in near-field downlink localization of a single-antenna user equipment (UE) using a single-antenna base station (BS) with the help of ARIS. Specifically, the unknown element-wise channel amplitudes of ARIS are hard to estimate due to the large size of ARIS. On the other hand, the variation in amplitudes is often negligible on small scales of ARIS. Based on this observation, we define sub-ARIS regions where the amplitudes of the elements are assumed or approximated to be identical. This simplification effectively reduces the number of parameters to estimate while still enabling accurate localization capability. Hence, our *sub-region based modeling approach* serves to bridge the gap between the prohibitive complexity of *full-fledged near-field models* incorporating channel spatial non-stationarity (SNS) effects into all ARIS elements and the *over-simplicity of near-field models with no SNS effects* (i.e., identical channel amplitudes over the entire ARIS). Furthermore, we optimize ARIS codebook based on the proposed sub-region based model, improving near-field localization performance. The key novelty and contributions of this article can thus be stated and summarized as follows:

- **Sub-region Based Misspecified Model:** We propose a sub-region based model to reduce the number of unknowns related to ARIS elements' channel amplitudes while still maintaining high localization performance with low pilot overhead. This facilitates near-optimal estimation of parameters under a model misspecification between the full-fledged near-field model and the proposed misspecified model.
- **Low-Complexity Localization Algorithm:** To tackle the infeasibility of solving the localization problem with the full-fledged model, we propose a low-complexity near-field localization algorithm based on mismatched maximum likelihood (MML) estimation that relies on the proposed sub-region based misspecified model. Numerical evaluations show that the proposed algorithm achieves localization accuracy closely aligned with the theoretical lower bounds.
- **Analysis Through MCRB:** The degree of model misspecification depends on the assumed number of sub-ARIS regions. To quantify the resulting performance degradation in ARIS-aided near-field localization, we conduct a comprehensive MCRB analysis that highlights the impact of model misspecification on localization accuracy and provides practical guidelines for selecting an appropriate number of sub-ARISs. The results demonstrate that choosing a proper number of sub-ARISs can yield location estimates with negligible performance loss.
- **ARIS Codebook Optimization:** To enhance the localization performance of the proposed algorithm, we design ARIS codebooks under coarse UE location knowledge by combining spatially-focused and derivative beams. The results demonstrate significant gains over codebooks consisting of spatially-focused beams and random codebook, particularly at low transmit powers, where accuracy improvements are most critical. Moreover, the proposed codebook exhibits strong robustness to multipath effects.

Notations: Vectors and matrices are presented in bold lowercase and uppercase letters, respectively. Sets are represented by calligraphic uppercase letters. The m-th element of a vector $\mathbf{a}$ is denoted as $[\mathbf{a}]_m$, while a submatrix of $\mathbf{J}$ spanning rows i to j and columns k to l is expressed as $[\mathbf{J}]_{[i:j,k:l]}$. The operators for Hermitian transpose, transpose, pseudoinverse, and complex conjugation are denoted by $(\cdot)^H$, $(\cdot)^\top$, $(\cdot)^\dagger$, and $(\cdot)^*$, respectively. The L2 norm operator is $\|\cdot\|$, and the argument for a complex number is defined as $\arg(\cdot)$. $\Re\{\beta\}$ extracts the real component(s) of complex input β. The Kronecker product is presented by $\otimes$ and the trace of a matrix $\mathbf{X}$ is denoted by $\mathrm{Tr}(\mathbf{X})$. Element-wise multiplication is expressed using $\odot$, and summation is indicated by $\sum$. Matrix inequalities are denoted by $\succeq$. The covariance operator is represented by $\mathrm{Cov}(\cdot)$ while $\langle\cdot\rangle$ represents the average over vector elements. Finally, the operator $|\cdot|$ denotes the complex modulus.

II. System Model and Problem Formulation

A. Basics and Problem Geometry

We consider a downlink single-input single-output (SISO) scenario where we aim to localize a UE based on signals transmitted by a BS, as shown in Fig. 1. The BS and UE

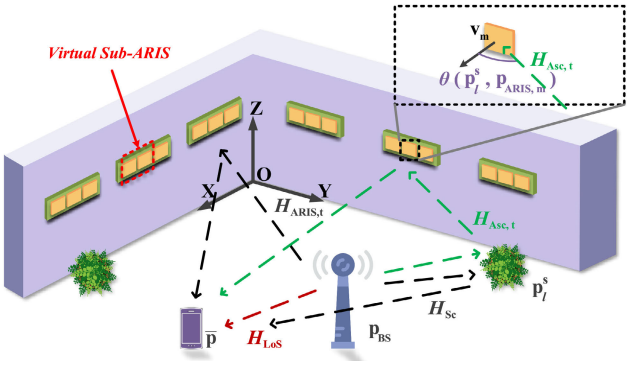

Fig. 1. Illustration of the considered RIS-aided localization scenario where a large multi-panel ARIS is deployed on the walls. The propagation paths of line-of-sight (LoS), first-order reflections, and second-order reflections are marked by red, black, and green dashed arrows, respectively. The red dashed frame marks an example virtual sub-ARIS region, whose size can in general vary from a fragment of a single physical panel to a set of adjacent physical panels depending on the parameterization of the proposed estimator.

are both equipped with an omnidirectional antenna. Multiple physical ARIS panels are deployed and synchronized with the BS, serving as additional anchors to reflect the signal from the BS to the UE. The overall ARIS consists of a total of M elements, where the elements within a single physical panel are linearly placed on the wall with an element spacing of $\lambda_c/2$, where $\lambda_c = c/f_c$ is the wavelength corresponding to the carrier frequency f_c while c represents the speed of light. Furthermore, in the Cartesian system, we denote the known location of BS as $\mathbf{p}_{\text{BS}} = [x_{\text{BS}}, y_{\text{BS}}, z_{\text{BS}}]^\top \in \mathbb{R}^3$. Likewise, the known location of the m-th ARIS element and the unknown location of the UE are expressed as $\mathbf{p}_{\text{ARIS},m} = [x_{\text{ARIS},m}, y_{\text{ARIS},m}, z_{\text{ARIS},m}]^\top \in \mathbb{R}^3$, and $\overline{\mathbf{p}} = [\overline{x}, \overline{y}, \overline{z}]^\top \in \mathbb{R}^3$, respectively. We also assume L unknown scatterers randomly located in the environment with locations $\mathbf{p}_l^s = [x_l^s, y_l^s, z_l^s]^\top \in \mathbb{R}^3, \forall l \in \{1, 2, \ldots, L\}$.

B. Signal and Channel Model

We assume and consider a narrowband transmission model, which can, in practice, represent a single sub-carrier in an orthogonal frequency division multiplexing (OFDM)-based system. The BS transmits constant amplitude pilot symbols $s_t \in \mathbb{C}$ to UE at instances $t \in \{0, 1, \ldots, 2T-1\}$, with a bandwidth W and transmit power $P_t = WE_s$, where $E_s = \mathbb{E}\{|s|^2\}$ is the energy per symbol. Here, T denotes the effective pilot number used to extract measurements for localization; further explanation is provided later in this section. The received signal at UE is given by

$$y_t = (H_{\text{LoS}} + H_{\text{Sc}} + H_{\text{ASc},t} + H_{\text{ARIS},t})s_t + n_t, \tag{1}$$

where $n_t \in \mathbb{C}$ is independent identically distributed (i.i.d.) complex Gaussian noise with zero mean and variance (in dB) $N_0 = -174 + 10\log_{10}(W) + NF$, where $-174\,\text{dBm/Hz}$ is the thermal noise density at room temperature, W is the bandwidth in Hertz, and NF is the receiver noise figure in dB. The channel response of the LoS path is denoted by H_{LoS}, while the first-order reflection path from scatterers and ARIS are denoted by H_{Sc} and $H_{\text{ARIS},t}$, respectively. The second-order reflection path, denoted with $H_{\text{ASc},t}$, includes both Tx-ARIS-scatterers-Rx and Tx-scatterers-ARIS-Rx paths. All four channel components are described by

$$H_{\text{LoS}} = e^{j\overline{\psi}} \frac{\lambda_c}{4\pi\|\mathbf{p}_{\text{BS}} - \overline{\mathbf{p}}\|} e^{-j\frac{2\pi}{\lambda_c}(\|\mathbf{p}_{\text{BS}} - \overline{\mathbf{p}}\|)}, \tag{2}$$

$$H_{\text{Sc}} = e^{j\overline{\psi}} \sum_{l=1}^{L} \beta_l^{\text{Sc}} e^{-j\varphi_l^{\text{Sc}}}, \tag{3}$$

$$H_{\text{ARIS},t} = e^{j\overline{\psi}} \mathbf{a}^\top(\mathbf{p}_{\text{BS}}) \text{diag}(\boldsymbol{\beta} \odot \boldsymbol{\omega}_t) \mathbf{a}(\overline{\mathbf{p}}), \tag{4}$$

$$H_{\text{ASc},t} = e^{j\overline{\psi}} \boldsymbol{\omega}_t^\top \sum_{l=1}^{L} (\boldsymbol{\beta}_l^{\text{ASc}} \odot e^{-j\boldsymbol{\varphi}_l^{\text{ASc}}} + \boldsymbol{\beta}_l^{\text{ScA}} \odot e^{-j\boldsymbol{\varphi}_l^{\text{ScA}}}), \tag{5}$$

where $\overline{\psi} \in (-\pi, \pi]$ is the phase offset between the BS and the UE. The coefficients β_l^{Sc} and φ_l^{Sc} in Equation (3) are channel amplitude and phase of the Tx-scatterer-Rx path, and their values can be defined and computed as

$$\beta_l^{\text{Sc}} = \frac{\sqrt{\sigma_{\text{RCS}}}\lambda_c^2}{8\pi^{1.5}\|\mathbf{p}_{\text{BS}} - \mathbf{p}_l^s\|\|\overline{\mathbf{p}} - \mathbf{p}_l^s\|}, \tag{6}$$

$$\varphi_l^{\text{Sc}} = \frac{2\pi}{\lambda_c}(\|\mathbf{p}_{\text{BS}} - \mathbf{p}_l^s\| + \|\overline{\mathbf{p}} - \mathbf{p}_l^s\|), \tag{7}$$

where σ_{RCS} is the radar cross-section of scatterers.

In the first-order reflection channel of ARIS, $H_{\text{ARIS},t}$, $\boldsymbol{\omega}_t \in \mathbb{C}^M$ is the ARIS coefficient vector at instant t. The m-th element of the reflection coefficient $\boldsymbol{\omega}_t$ is $\omega_{m,t} = \rho_{m,t}e^{j\varphi_{m,t}}$, where $\varphi_{m,t} \in (0, \pi]$ is the phase and $\rho_{m,t} \in [0, 1]$ is the amplitude [13]. We can describe the ARIS steering vector as $\mathbf{a}(\mathbf{q}) \in \mathbb{C}^M$, whose m-th entry reads

$$[\mathbf{a}(\mathbf{q})]_m = e^{-j\frac{2\pi}{\lambda_c}\|\mathbf{q} - \mathbf{p}_{\text{ARIS},m}\|}, \tag{8}$$

where $\mathbf{q} \in \{\overline{\mathbf{p}}, \mathbf{p}_{\text{BS}}\}$. For the channel amplitude, we define the vector $\boldsymbol{\beta} \in \mathbb{R}_{>0}^M$ to describe the link from BS to UE via the ARIS. The m-th entry of ARIS's amplitude vector is expressed as [39]

$$[\boldsymbol{\beta}]_m = \frac{\sqrt{G(\overline{\mathbf{p}}, \mathbf{p}_{\text{BS}}, \mathbf{p}_{\text{ARIS},m})}(\lambda_c/2)^2}{4\pi\|\overline{\mathbf{p}} - \mathbf{p}_{\text{ARIS},m}\|\|\mathbf{p}_{\text{BS}} - \mathbf{p}_{\text{ARIS},m}\|}, \tag{9}$$

where $G(\mathbf{q}_1, \mathbf{p}_{\text{ARIS},m}, \mathbf{q}_2) \in \mathbb{R}$ is the function that computes m-th ARIS element gain regarding the signal that comes from the location $\mathbf{q}_1$ to the reflected location $\mathbf{q}_2$. This is defined based on [39] as

$$G(\mathbf{q}_1, \mathbf{p}_{\text{ARIS},m}, \mathbf{q}_2) = \frac{\cos^2(\theta(\mathbf{q}_1, \mathbf{p}_{\text{ARIS},m}))\sin^2(\Delta(\mathbf{q}_1, \mathbf{p}_{\text{ARIS},m}, \mathbf{q}_2))}{\Delta^2(\mathbf{q}_1, \mathbf{p}_{\text{ARIS},m}, \mathbf{q}_2)}. \tag{10}$$

where $\Delta(\mathbf{q}_1, \mathbf{p}_{\text{ARIS},m}, \mathbf{q}_2)$ is the intermediate function that computes the sine difference between two angles, and $\theta(\mathbf{q}, \mathbf{p}_{\text{ARIS},m}) \in [0, 2\pi]$ denotes the signal propagation angle between two points with respect to the normalized vector $\mathbf{v}_m \in \mathbb{R}^3$, which is perpendicular to the plane of m-th ARIS element. These can be expressed as

$$\Delta(\mathbf{q}_1, \mathbf{p}_{\text{ARIS},m}, \mathbf{q}_2) = \frac{\pi}{2}\left(\sin(\theta(\mathbf{q}_2, \mathbf{p}_{\text{ARIS},m})) - \sin(\theta(\mathbf{q}_1, \mathbf{p}_{\text{ARIS},m}))\right), \tag{11}$$

$$\theta(\mathbf{q}, \mathbf{p}_{\text{ARIS},m}) = \arccos\left(\frac{(\mathbf{q} - \mathbf{p}_{\text{ARIS},m})^\top \mathbf{v}_m}{\|\mathbf{q} - \mathbf{p}_{\text{ARIS},m}\|}\right). \tag{12}$$

For second-order reflections, we have the channel amplitude $\boldsymbol{\beta}_l^{\mathrm{ASc}} \in \mathbb{R}^M$ and phase $\boldsymbol{\varphi}_l^{\mathrm{ASc}} \in \mathbb{R}^M$ of the Tx-ARIS-scatterer-Rx path. Similarly, $\boldsymbol{\beta}_l^{\mathrm{ScA}} \in \mathbb{R}^M$ and $\boldsymbol{\varphi}_l^{\mathrm{ScA}} \in \mathbb{R}^M$ are the channel amplitude and phase of the Tx-scatterer-ARIS-Rx path. The m-th entries of the above channel vectors can now be expressed as

$$[\boldsymbol{\beta}_l^{\mathrm{ASc}}]_m = \frac{\sqrt{G(\mathbf{p}_{\mathrm{BS}}, \mathbf{p}_{\mathrm{ARIS},m}, \mathbf{p}_l^s)\sigma_{\mathrm{RCS}}}(\lambda_c/2)^2}{8\pi^{1.5}\|\mathbf{p}_{\mathrm{BS}} - \mathbf{p}_{\mathrm{ARIS},m}\|\|\mathbf{p}_{\mathrm{ARIS},m} - \mathbf{p}_l^s\|\|\overline{\mathbf{p}} - \mathbf{p}_l^s\|}, \tag{13}$$

$$[\boldsymbol{\varphi}_l^{\mathrm{ASc}}]_m = \arg([\mathbf{a}(\mathbf{p}_{\mathrm{BS}})]_m) + \arg([\mathbf{a}(\mathbf{p}_l^s)]_m) - \frac{2\pi}{\lambda_c}\|\overline{\mathbf{p}} - \mathbf{p}_l^s\|, \tag{14}$$

$$[\boldsymbol{\beta}_l^{\mathrm{ScA}}]_m = \frac{\sqrt{G(\mathbf{p}_l^s, \mathbf{p}_{\mathrm{ARIS},m}, \overline{\mathbf{p}})\sigma_{\mathrm{RCS}}}(\lambda_c/2)^2}{8\pi^{1.5}\|\overline{\mathbf{p}} - \mathbf{p}_{\mathrm{ARIS},m}\|\|\mathbf{p}_{\mathrm{ARIS},m} - \mathbf{p}_l^s\|\|\mathbf{p}_{\mathrm{BS}} - \mathbf{p}_l^s\|}, \tag{15}$$

$$[\boldsymbol{\varphi}_l^{\mathrm{ScA}}]_m = \arg([\mathbf{a}(\overline{\mathbf{p}})]_m) + \arg([\mathbf{a}(\mathbf{p}_l^s)]_m) - \frac{2\pi}{\lambda_c}\|\mathbf{p}_{\mathrm{BS}} - \mathbf{p}_l^s\|. \tag{16}$$

To extract signals associated with the ARIS, we can design its reflection coefficients to form a balanced sequence. For example, setting $\boldsymbol{\omega}_t = -\boldsymbol{\omega}_{t+1}$, the corresponding channel response satisfies $H_{\mathrm{ARIS},t} = -H_{\mathrm{ARIS},t+1}$ for odd t. This design ensures that the sum of the ARIS-involved channels over the entire duration cancels out, i.e., $\sum_{t=1}^{2T} H_{\mathrm{ARIS},t} = 0$ [40], [41]. By substituting channel models at adjacent time instants, this approach enables cancellation of H_{LoS} and H_{Sc}, while maintaining the components associated with the ARIS. After that, the received signal $\mathbf{y} \in \mathbb{C}^T$, where T is the effective pilot number for localization purposes, can be expressed as

$$\mathbf{y} = e^{j\overline{\psi}}\mathbf{F}^\top(\boldsymbol{\beta} \odot \mathbf{a}(\overline{\mathbf{p}})) + \mathbf{y}_{\mathrm{INT}} + \mathbf{n}, \tag{17}$$

$$\mathbf{y}_{\mathrm{INT}} = e^{j\overline{\psi}}\boldsymbol{\Omega}^\top \sum_{l=1}^{L}(\boldsymbol{\beta}_l^{\mathrm{ASc}} \odot e^{-j\boldsymbol{\varphi}_l^{\mathrm{ASc}}} + \boldsymbol{\beta}_l^{\mathrm{ScA}} \odot e^{-j\boldsymbol{\varphi}_l^{\mathrm{ScA}}}), \tag{18}$$

where $\mathbf{F} = [\mathbf{f}_1, \ldots, \mathbf{f}_T] \in \mathbb{C}^{M\times T}$, $\mathbf{f}_\tau = \mathrm{diag}(\boldsymbol{\omega}_{2\tau-1})\mathbf{a}(\mathbf{p}_{\mathrm{BS}}) \in \mathbb{C}^M, \tau \in \{1, 2, \ldots, T\}$, $\mathbf{y}_{\mathrm{INT}} \in \mathbb{C}^T$ is the interference signal reflected from the scatterers, and $\boldsymbol{\Omega} = [\boldsymbol{\omega}_1, \boldsymbol{\omega}_3, \ldots, \boldsymbol{\omega}_{2T-1}] \in \mathbb{C}^{M\times T}$. The additive noise is $\mathbf{n} \sim \mathcal{CN}(\mathbf{0}, \rho\mathbf{I})$, where $\rho = N_0/(2E_s)$ denotes the normalized noise power relative to the symbol energy. The model in (17) is the full-fledged near-field model describing the true channel characteristics.

C. Problem Description

Our first main goal is to recover the UE position $\overline{\mathbf{p}}$ from the received signal $\mathbf{y}$ in (17). In an indoor scenario, the 2D location of the UE is our interest, hence, we simplify the problem by assuming a known height of the UE, and thus $\overline{\boldsymbol{\eta}} = [\overline{\mathbf{p}}_{[1:2]}, \overline{\psi}, \boldsymbol{\beta}] \in \mathbb{R}^{M+3}$ has $M+3$ unknowns to be estimated. However, estimating $M+3$ real unknowns is not feasible when $T \ll M+3$. To address this challenge, we propose and develop a localization algorithm based on a *misspecified model* that assumes a constant amplitude within a single sub-ARIS, reducing the number of unknown parameters. The effective size of sub-ARISs varies depending on the chosen partitioning strategy during estimation; it can range from a segment of a single physical panel, which introduces more unknowns and more accurate approximation, to multiple panels, which results in fewer unknowns and reduced accuracy. Notably, this flexible segmentation does not require modifications to the physical panels. Instead, it uses reasonable virtual partitioning across the overall ARIS entity within the estimation algorithm. This simplification introduces *model misspecification* referring to the discrepancy between the true (generative) model in (17) and the misspecified (assumed) model involved in estimation, for which traditional tools such as the Fisher information matrix (FIM) and CRB are no longer suitable. Consequently, we use and derive expressions for the MCRB [42] as a theoretical performance metric to quantify the impact of this model misspecification on the estimation accuracy and performance.[1]

Then, our second main goal is to optimize the codebook $\mathbf{F}$ to estimate all unknowns under misspecification of the model while enhancing the localization accuracy with prior UE location. To achieve this, we formulate the codebook optimization as a position error bound (PEB) minimization problem, leveraging prior knowledge of the UE location to design efficient $\mathbf{F}$. Furthermore, we extend the codebook optimization to account for uncertainties in the coarse UE location information by considering a set of possible locations and minimizing the worst-case PEB. This addresses the codebook optimization problem for practical scenarios where only coarse location information is available.

III. Proposed Localization Algorithm and MCRB-Based Performance Analysis

This section presents the proposed low-complexity localization algorithm based on the MML framework using a misspecified sub-region model. We also derive MCRB expressions to characterize the fundamental performance limits under the considered model misspecification.

A. Sub-Region Based Misspecified Model

As the true element-wise channel amplitude vector $\boldsymbol{\beta}$ cannot be fully estimated in practice, the proposed approach assumes or considers the whole ARIS structure to be composed of K virtual sub-ARISs ($M \geq K \geq 1$) with the elements' channel gains within any individual sub-ARIS being mutually equal. This assumption or approximation is motivated by far-field RIS and large antenna array models, where equal amplitude and varying phase are commonly assumed [44]. Although such an assumption does not hold strictly in near-field propagation [45], it becomes increasingly accurate when each sub-ARIS spans a sufficiently small region where amplitude variations are mild [32]. From the modeling perspective, a coarse knowledge of the amplitude variation can be obtained through electromagnetic simulations or calibration, allowing sub-ARIS

[1] As for the biased CRB, it is in general formulated for analyzing estimation performance with a known bias and is thus not connected to any mismatch between the assumed and true signal models [43, Sec. 4.2.2]. Hence, it is not the most appropriate framework for our work, where the bias arises directly from model misspecification.

regions to be defined such that the intra-region amplitude differences remain below a chosen limit. Furthermore, from an estimation viewpoint, when the number of pilots T is smaller than the total number of ARIS elements M, estimating all individual amplitudes becomes infeasible, and grouping them into K sub-ARIS regions provides a practical trade-off between model accuracy and complexity. Further discussion and aspects related to how to choose the value of K are provided in Section III-E.

Now, for any given overall ARIS structure, we can define the K unknown amplitudes as $\boldsymbol{b} = [b_1, \ldots, b_K] \in \mathbb{R}^K_{>0}$. Consequently, we have the element-wise channel gain vector $\mathbf{b}_v \in \mathbb{R}^M$ which reads

$$\mathbf{b}_v = \mathbf{b} \otimes \mathbf{1}_{M/K}, \tag{19}$$

whose M/K entries of k-th sub-ARIS are equal to b_k. In addition, without knowing the location of the scatterers, $\mathbf{y}_{\text{INT}}$ in (18) is unknown to the receiver. Then, the misspecified model from the receiver's perspective becomes

$$\mathbf{y} \approx e^{j\psi}\mathbf{F}^\top(\mathbf{a}(\mathbf{p}) \odot \mathbf{b}_v) + \mathbf{n}, \tag{20}$$

where we use $\mathbf{p}$ and ψ as the *misspecified parameters* instead of $\overline{\mathbf{p}}$ and $\overline{\psi}$ that are the parameters of the true (regenerative) model in (17). The related theoretical analysis tools in terms of the MCRB for the estimated parameters under model misspecification will be discussed in Section III-C.

By defining a joint function $\mathbf{A}(\mathbf{p}) \in \mathbb{C}^{T\times K}$ incorporating both the codebook $\mathbf{F}$ and the steering vector $\mathbf{a}(\mathbf{p})$, we can next rewrite the misspecified model for a better representation of the unknowns. This is expressed as

$$\mathbf{y} \approx e^{j\psi}\mathbf{A}(\mathbf{p})\mathbf{b} + \mathbf{n}, \tag{21}$$

where

$$[\mathbf{A}(\mathbf{p})]_{[\tau,k]} = [\mathbf{F}^\top]_{\left[\tau, \frac{M(k-1)}{K}+1:\frac{Mk}{K}\right]}\mathbf{a}^{(k)}(\mathbf{p}), \tag{22}$$

and $\mathbf{a}^{(k)}(\mathbf{p}) = [\mathbf{a}(\mathbf{p})]_{\left[\frac{M(k-1)}{K}+1:\frac{Mk}{K}\right]} \in \mathbb{C}^{M/K}$ is the steering vector of the k-th sub-ARIS, with M/K denoting the number of elements in each sub-ARIS. When $K = 1$, the matrix simplifies to $\mathbf{A}(\mathbf{p}) = \mathbf{F}^\top\mathbf{a}(\mathbf{p})$, and $\mathbf{b}$ becomes a scalar, as discussed, e.g., in [34].

B. Localization Algorithm

Building on the above models, and assuming that the condition $K + 3 < T$ holds, we can now derive and express the associated maximum likelihood estimator, as

$$\mathcal{L}_1(\mathbf{y}|\mathbf{b}, \mathbf{p}, \psi) = \|\mathbf{y} - e^{j\psi}\mathbf{A}(\mathbf{p})\mathbf{b}\|^2, \tag{23}$$

and

$$\widehat{\mathbf{b}}, \widehat{\mathbf{p}}, \widehat{\psi} = \arg\min_{\mathbf{b},\mathbf{p},\psi} \mathcal{L}_1(\mathbf{y}|\mathbf{b}, \mathbf{p}, \psi). \tag{24}$$

This estimation problem involves a large number of parameters, including $\mathbf{p}$, ψ, and $\mathbf{b}$. Optimizing all parameters simultaneously is computationally expensive, and it is difficult to define a comprehensive and efficient search grid for $\mathbf{b}$. Thus, to effectively solve (24), we break the problem into lower-dimensional sub-problems. Specifically, for a given location $\mathbf{p}$, we first derive the stationary conditions for $\mathbf{b}(\mathbf{p})$ and $\psi(\mathbf{p})$ by taking the first-order derivatives of the loss function and setting them to zero. This leads to the following expressions of the form

$$\mathbf{b}(\mathbf{p}) = \Re\{\mathbf{A}(\mathbf{p})^H\mathbf{A}(\mathbf{p})\}^{-1}\Re\{\mathbf{A}(\mathbf{p})^H e^{-j\psi(\mathbf{p})}\mathbf{y}\}, \tag{25}$$

$$\psi(\mathbf{p}) = -\arg(\mathbf{y}^H\mathbf{A}(\mathbf{p})\mathbf{b}(\mathbf{p})). \tag{26}$$

Substituting then (26) into (23) leads to a reduced loss function of the form

$$\mathcal{L}_2(\psi; \mathbf{p}) = \|\mathbf{v} - e^{2j\psi}\mathbf{w}\|^2, \tag{27}$$

where $\mathbf{v} = \mathbf{y} - \mathbf{A}(\mathbf{p})\left(\Re\left\{\mathbf{A}^H(\mathbf{p})\mathbf{A}(\mathbf{p})\right\}\right)^{-1}\mathbf{A}^H(\mathbf{p})\mathbf{y}/2$ and $\mathbf{w} = \mathbf{A}(\mathbf{p})\left(\Re\left\{\mathbf{A}^H(\mathbf{p})\mathbf{A}(\mathbf{p})\right\}\right)^{-1}\mathbf{A}^\top(\mathbf{p})\mathbf{y}^*/2$. Minimizing (27) with respect to ψ yields a new closed-form estimate, expressed as

$$\psi(\mathbf{p}) = \arg(\mathbf{w}^H\mathbf{v})/2. \tag{28}$$

We then further substitute $\psi(\mathbf{p})$ back into (25) to obtain $\mathbf{b}(\mathbf{p})$ [2]

The closed-form solutions to find $\psi(\mathbf{p})$ and $\mathbf{b}(\mathbf{p})$ are based on $\mathbf{p}$, and thus a grid search over possible positions $\mathbf{p}_g \in \mathcal{P}$ is unavoidable. For each point on the grid $\mathcal{P}$, we use (25), and (28) to update $\psi(\mathbf{p}_g)$ and $\mathbf{b}(\mathbf{p}_g)$. The detailed steps for the proposed overall estimator approach are outlined and summarized in Algorithm 1.

Algorithm 1 Proposed MML Estimator to Solve (24)

1: Initialize: Position grid $\mathcal{P}$, number of virtual sub-ARISs K
2: **for** $\forall \mathbf{p}_g \in \mathcal{P}$ **do**
3: $\quad\mathbf{A}(\mathbf{p}_g) \leftarrow$ (22)
4: $\quad\widehat{\psi}(\mathbf{p}_g) \leftarrow$ (28)
5: $\quad\widehat{\mathbf{b}}(\mathbf{p}_g) \leftarrow$ (25)
6: $\quad\delta(\mathbf{p}_g) \leftarrow \left\|\mathbf{y} - e^{j\widehat{\psi}(\mathbf{p}_g)}\mathbf{A}(\mathbf{p}_g)\widehat{\mathbf{b}}(\mathbf{p}_g)\right\|^2$
7: **end for**
8: $\widehat{\mathbf{p}} \leftarrow \arg\min_{\mathbf{p}_g\in\mathcal{P}} \delta(\mathbf{p}_g)$
9: Compute $\widehat{\mathbf{b}}(\widehat{\mathbf{p}})$, $\widehat{\psi}(\widehat{\mathbf{p}})$

C. MCRB Derivation

To quantify and assess the fundamental estimation error bound of the proposed MML estimator with a model misspecification, we next derive the MCRB for the misspecified model. Let us start with the true model in (17) regarding the unknown parameter vector $\overline{\boldsymbol{\eta}} = [\overline{\mathbf{p}}_{[1:2]}, \overline{\psi}, \boldsymbol{\beta}]$. Then, we set the noise-free component of $\mathbf{y}$ as $\boldsymbol{\mu}(\overline{\boldsymbol{\eta}}) = e^{j\overline{\psi}}\mathbf{F}^\top(\boldsymbol{\beta}\odot\mathbf{a}(\overline{\mathbf{p}}))+\mathbf{y}_{\text{INT}}$, and can express the probability density function (PDF) and log-likelihood function (LLF) of the true observation as

$$p(\mathbf{y}|\overline{\boldsymbol{\eta}}) = \frac{1}{\pi N_0}e^{-\frac{\|\mathbf{y}-\boldsymbol{\mu}(\overline{\boldsymbol{\eta}})\|^2}{N_0}}, \tag{29}$$

$$\log\, p(\mathbf{y}|\overline{\boldsymbol{\eta}}) = -\log\,(\pi N_0) - \frac{\|\mathbf{y}-\boldsymbol{\mu}(\overline{\boldsymbol{\eta}})\|^2}{N_0}. \tag{30}$$

[2]Note that, since (27) is a function of 2ψ, the effective estimation range of ψ becomes $[-\pi/2, \pi/2]$. Values of ψ out of this interval introduce a sign ambiguity in the estimated $\mathbf{b}(\mathbf{p})$. This ambiguity can be resolved by enforcing a non-negative representation of $\mathbf{b}(\mathbf{p})$, such as using its magnitude $|\mathbf{b}(\mathbf{p})|$ and recomputing $\psi(\mathbf{p})$ accordingly.

Similarly, the PDF and the LLF for misspecified parameters $\boldsymbol{\eta}$ can be expressed as

$$\tilde{p}(\mathbf{y}|\boldsymbol{\eta}) = \frac{1}{\pi N_0} e^{-\frac{\|\mathbf{y}-\tilde{\boldsymbol{\mu}}(\boldsymbol{\eta})\|^2}{N_0}}, \tag{31}$$

$$\log \tilde{p}(\mathbf{y}|\boldsymbol{\eta}) = -\log(\pi N_0) - \frac{\|\mathbf{y}-\tilde{\boldsymbol{\mu}}(\boldsymbol{\eta})\|^2}{N_0}, \tag{32}$$

where $\tilde{\boldsymbol{\mu}}(\boldsymbol{\eta}) = e^{j\psi}\mathbf{F}^\top(\mathbf{a}(\mathbf{p})\odot\mathbf{b}_v)$ is the noise-free component of the misspecified model.

Now, to derive the MCRB associated with the model misspecification between (29) and (20), we firstly need to identify the pseudo-true parameter vector

$$\mathring{\boldsymbol{\eta}} = \left[\mathring{\mathbf{p}}_{[1:2]}, \mathring{\psi}, \mathring{\mathbf{b}}\right] \in \mathbb{R}^{K+3}, \tag{33}$$

and compute the MCRB of it. This vector is computed by minimizing the Kullback-Leibler (KL) divergence between the two models' PDFs. Specifically, we express this as

$$\mathring{\boldsymbol{\eta}} = \arg\min_{\boldsymbol{\eta}} D(p(\mathbf{y})\|\tilde{p}(\mathbf{y}|\boldsymbol{\eta})), \tag{34}$$

where $D(p(\mathbf{y})\|\tilde{p}(\mathbf{y}|\boldsymbol{\eta})) = \int_{\infty}^{\infty} p(\mathbf{y})\log\frac{p(\mathbf{y})}{\tilde{p}(\mathbf{y}|\boldsymbol{\eta})}\,d\mathbf{y}$ represents the KL divergence between the true and misspecified models' densities. As derived in [36, Appendix A], $\mathring{\boldsymbol{\eta}}$ is the pseudo-true parameter vector leading to the minimal Euclidean distance between two models in Equations (17) and (20). This can thus be expressed as

$$\mathring{\boldsymbol{\eta}} = \arg\min_{\boldsymbol{\eta}} \sum_{t=1}^{T} \|\tilde{\mu}_t(\boldsymbol{\eta}) - \mu_t\|^2. \tag{35}$$

The pseudo-true parameter $\mathring{\boldsymbol{\eta}}$ is estimated using the proposed mismatched maximum likelihood approach with noise-free signals. Since this step is part of the bound computation, we can use the true value as the initial guess for the optimization.

Following this, the MCRB matrix [36], [42] corresponding to $\mathring{\boldsymbol{\eta}}$ can now be computed as

$$\text{MCRB}(\mathring{\boldsymbol{\eta}}) = \mathbf{P}_{\mathring{\boldsymbol{\eta}}}^{-1}\mathbf{B}_{\mathring{\boldsymbol{\eta}}}\mathbf{P}_{\mathring{\boldsymbol{\eta}}}^{-1} \quad \in \mathbb{R}^{(K+3)\times(K+3)}. \tag{36}$$

Here, the (i,j)-th elements of matrices $\mathbf{P}_{\mathring{\boldsymbol{\eta}}}$ and $\mathbf{B}_{\mathring{\boldsymbol{\eta}}}$ are defined as

$$[\mathbf{P}_{\mathring{\boldsymbol{\eta}}}]_{i,j} = \mathbb{E}_p\left\{\frac{\partial^2}{\partial\eta_i\partial\eta_j}\log(\tilde{p}(\mathbf{y}|\boldsymbol{\eta}))\Big|_{\boldsymbol{\eta}=\mathring{\boldsymbol{\eta}}}\right\}, \tag{37}$$

$$[\mathbf{B}_{\mathring{\boldsymbol{\eta}}}]_{i,j} = \mathbb{E}_p\left\{\frac{\partial\log(\tilde{p}(\mathbf{y}|\boldsymbol{\eta}))}{\partial\eta_i}\frac{\partial\log(\tilde{p}(\mathbf{y}|\boldsymbol{\eta}))}{\partial\eta_j}\Big|_{\boldsymbol{\eta}=\mathring{\boldsymbol{\eta}}}\right\}. \tag{38}$$

After some algebraic manipulations, the compact forms of $\mathbf{P}_{\mathring{\boldsymbol{\eta}}}$ and $\mathbf{B}_{\mathring{\boldsymbol{\eta}}}$ can be derived to read

$$[\mathbf{P}_{\mathring{\boldsymbol{\eta}}}]_{i,j} = \frac{2}{N_0}\Re\left\{\boldsymbol{\epsilon}(\boldsymbol{\eta})^H\frac{\partial^2\tilde{\boldsymbol{\mu}}(\boldsymbol{\eta})}{\partial\eta_i\partial\eta_j} - \frac{\partial\tilde{\boldsymbol{\mu}}(\boldsymbol{\eta})^H}{\partial\eta_i}\frac{\partial\tilde{\boldsymbol{\mu}}(\boldsymbol{\eta})}{\partial\eta_j}\right\}\Big|_{\boldsymbol{\eta}=\mathring{\boldsymbol{\eta}}}, \tag{39}$$

$$[\mathbf{B}_{\mathring{\boldsymbol{\eta}}}]_{i,j} = \frac{2}{N_0}\Big[\frac{2}{N_0}\Re\left\{\boldsymbol{\epsilon}(\boldsymbol{\eta})^H\frac{\partial\tilde{\boldsymbol{\mu}}(\boldsymbol{\eta})}{\partial\eta_i}\right\}\Re\left\{\boldsymbol{\epsilon}(\boldsymbol{\eta})^H\frac{\partial\tilde{\boldsymbol{\mu}}(\boldsymbol{\eta})}{\partial\eta_j}\right\} + \Re\left\{\frac{\partial\tilde{\boldsymbol{\mu}}(\boldsymbol{\eta})^H}{\partial\eta_i}\frac{\partial\tilde{\boldsymbol{\mu}}(\boldsymbol{\eta})}{\partial\eta_j}\right\}\Big]\Big|_{\boldsymbol{\eta}=\mathring{\boldsymbol{\eta}}}, \tag{40}$$

where $\boldsymbol{\epsilon}(\boldsymbol{\eta}) = \boldsymbol{\mu} - \tilde{\boldsymbol{\mu}}(\boldsymbol{\eta})$ is the bias term reflecting the difference between the two models.

For indoor scenarios, as already noted, we are primarily interested in the UE's 2D location. Thus, assuming a known UE height, we extract the $\text{MCRB}_{[1:2,1:2]}$ corresponding to 2D coordinates, representing the MCRB of the pseudo-true location $\mathring{\mathbf{p}}$. In practice, $\text{MCRB}_{[1:2,1:2]}$ serves as a lower bound for the covariance of any misspecified unbiased estimator regarding the true parameter $\overline{\mathbf{p}}$ [42]. The final expression for the lower bound reads now

$$\text{LB}(\overline{\boldsymbol{\eta}}) = \text{MCRB}_{[1:2,1:2]} + (\overline{\mathbf{p}}_{[1:2]} - \mathring{\mathbf{p}}_{[1:2]})(\overline{\mathbf{p}}_{[1:2]} - \mathring{\mathbf{p}}_{[1:2]})^\top. \tag{41}$$

The second term represents the covariance of the difference between the pseudo-true location vector $\mathring{\mathbf{p}}$ and the true location vector $\overline{\mathbf{p}}$. Thus, the error covariance of the MML estimator is bounded by the MCRB, and the mean squared error (MSE) of that estimator is bounded by the derived lower bound (LB).

Since MCRB and LB are expressed in squared meters, we take their square roots to obtain theoretical references for comparison with root mean squared error (RMSE) metric. The key theoretical performance metrics are thus eventually

$$\text{MPEB} = \sqrt{\text{Tr}\{\text{MCRB}_{[1:2,1:2]}\}}, \tag{42}$$

$$\text{BPEB} = \sqrt{\text{Tr}\{\text{LB}\}}, \tag{43}$$

$$\text{RPB} = \sqrt{\text{Tr}\{(\overline{\mathbf{p}}_{[1:2]} - \mathring{\mathbf{p}}_{[1:2]})(\overline{\mathbf{p}}_{[1:2]} - \mathring{\mathbf{p}}_{[1:2]})^\top\}}, \tag{44}$$

where misspecified position error bound (MPEB) and biased position error bound (BPEB) represent the theoretical limit on RMSE regarding the pseudo-true location $\mathring{\mathbf{p}}$ and true location $\overline{\mathbf{p}}$, respectively. Moreover, the square root of the estimated location bias is quantified by root of position bias (RPB). Then, the expression in (41) can be rewritten or expressed as

$$\text{BPEB}^2 = \text{MPEB}^2 + \text{RPB}^2. \tag{45}$$

Finally, to evaluate the practical performance of the estimator, we compute RMSE corresponding to $\mathring{\mathbf{p}}$ and $\overline{\mathbf{p}}$ as

$$\text{RMSE}(\mathbf{p}_{\text{temp}}) = \sqrt{\frac{1}{R}\sum_{i=1}^{R}(\widehat{\mathbf{p}} - \mathbf{p}_{\text{temp}})^2}, \tag{46}$$

where $\mathbf{p}_{\text{temp}} \in \{\mathring{\mathbf{p}}, \overline{\mathbf{p}}\}$.

D. Complexity Analysis

The computational complexity to solve the problem in (23) depends on the number of position candidates in the grid, denoted by $\mathcal{P}$, and the assumed number of amplitudes, K. The complexity related to every point is relative to $\mathcal{O}(MK^2+K^3)$. Taking into account $\mathcal{P}$, we have thus the overall complexity in the order of $\mathcal{O}(\mathcal{P}(MK^2+K^3))$.

E. Choosing the Value of K

In general, the value of K impacts the misspecified model and consequently the estimator performance and the related bounds, thus choosing the value of K is an important practical aspect. As the optimum or well-performing value(s) of K cannot be trivially known in advance, such must in general be chosen based on reasonable physical assumptions and

reasoning related to the ARIS deployment scenario–perhaps combined with some further engineering insight. In general, we propose that the selection of K can be guided by prior experimental or model-based knowledge of the spatial amplitude variation across the ARIS elements together with the required positioning accuracy. In practice, coarse information about amplitude non-uniformity can be obtained either from channel models or from offline calibration measurements. Based on this knowledge, the ARIS can be partitioned into virtual sub-regions such that the amplitude variations within each sub-ARIS remain within a tolerable range (e.g., within $2-3\,\mathrm{dB}$). This provides a practical heuristic approach: one can use model-based or measured amplitude datasets to determine the largest contiguous regions that satisfy the 2 or $3\,\mathrm{dB}$ criterion and set K accordingly.

Alternatively, and importantly, we highlight that the derived BPEB and position bias norm also offer a way to obtain insight into the impact of K in any given environment or deployment scenario. More specifically, one can compute the bounds for the given scenario, for different values of K, and pursue further with such a value that provides sufficiently low bounds at practically meaningful (sufficiently high) transmit power levels where the bounds and RMSEs are closely matching (cf. the numerical results in Section V). Specifically, K can be selected such that the norm of the position bias remains below a threshold corresponding to the required localization accuracy. Based on these two criteria, we can define the following selection rules for K using the BPEB and the RPB, expressed as

$$K^{\star}_{\text{BPEB}} = \min\left\{K \in \mathcal{K} : \text{BPEB}(K) \le \varepsilon_{\text{BPEB}}\right\}, \tag{47}$$

$$K^{\star}_{\text{RPB}} = \min\left\{K \in \mathcal{K} : \text{RPB}(K) \le \varepsilon_{\text{RPB}}\right\}. \tag{48}$$

Here, $\mathcal{K}$ denotes the set of candidate partition numbers (e.g., $\mathcal{K} = \{1, 2, \ldots, K_{\max}\}$), while $\varepsilon_{\text{BPEB}}$ and ε_{RPB} are user-defined thresholds that specify the acceptable levels of biased position error bound and position bias norm, respectively, according to the desired localization accuracy (e.g., in centimeters or meters). The obtained values $K^{\star}_{\text{BPEB}}$ and $K^{\star}_{\text{RPB}}$ thus represent the criterion-wise optimal K selections, from which the smaller one indicates the optimal K that satisfies both criteria.

IV. Codebook Design

In this section, we propose a codebook design method to enhance localization performance by minimizing the PEB, based on the misspecified model in (20). Since the optimization process requires knowledge of the UE location, we describe and formulate solutions for both perfect and imperfect location knowledge situations.

A. FIM and PEB

To minimize the PEB, we firstly derive and express the conventional FIM $\mathbf{J}_K(\boldsymbol{\eta})$ with respect to $\boldsymbol{\eta}$ as

$$\mathbf{J}_K(\boldsymbol{\eta}) = \frac{2}{\rho}\Re\left\{\left(\frac{\partial\tilde{\boldsymbol{\mu}}}{\partial\boldsymbol{\eta}}\right)^H \frac{\partial\tilde{\boldsymbol{\mu}}}{\partial\boldsymbol{\eta}}\right\} \in \mathbb{R}^{(K+3)\times(K+3)}. \tag{49}$$

Since the UE's 2D location is of our interest, the PEB can then be expressed as

$$\text{PEB}_K(\mathbf{F}, \boldsymbol{\eta}) = \sqrt{\text{Tr}([\mathbf{J}_K^{-1}(\boldsymbol{\eta})]_{(1:2,1:2)})}, \tag{50}$$

where PEB has explicit dependence on the codebook matrix $\mathbf{F}$.

B. PEB Minimization Based Codebook Design

Assuming prior knowledge of UE's position, the PEB optimization problem under a codebook's power constraint can be formulated as

$$\begin{aligned} &\min_{\mathbf{F}} \text{PEB}_K(\mathbf{F}, \boldsymbol{\eta}) \\ &\text{s.t.} \quad \text{Tr}(\mathbf{F}\mathbf{F}^H) \le MT, \end{aligned} \tag{51}$$

where MT is the upper bound of power constraint for the ARIS codebook.

By defining the codebook's covariance matrix as $\mathbf{X} = \mathbf{F}\mathbf{F}^H$, we can find that the FIM's elements in (50) are linear functions of $\mathbf{X}$. Consequently, PEB is a convex function of $\mathbf{X}$. Following the Trace-Opt criterion in [46, Chapter 7.5.2], the optimization problem in (51) can be reformulated as a semi-definite programming (SDP) problem or task focusing on 2D locations as

$$\begin{aligned} \min_{\mathbf{X},\mathbf{u}} \quad & \mathbf{1}^\top \mathbf{u} \\ \text{s.t.} \quad & \begin{bmatrix} \mathbf{J}_K(\boldsymbol{\eta}) & \mathbf{e}_g \\ \mathbf{e}_g & \mathbf{u}_g \end{bmatrix} \succeq 0, \quad g = 1, 2, \\ & \mathbf{X} \succ 0, \\ & \text{Tr}(\mathbf{X}) \le MT, \end{aligned} \tag{52}$$

where $\mathbf{u} = [u_1, u_2]$ is the auxiliary variable vector corresponding to the 2D coordinates x and y. Here, $\mathbf{e}_g$ represents the g-th column of a $(K+3)\times(K+3)$ identity matrix.

Proposition 1: The optimal covariance matrix of the codebook can be represented as

$$\mathbf{X}^* = \mathbf{U}\boldsymbol{\Lambda}\mathbf{U}^H. \tag{53}$$

The structure of $\mathbf{U}$ and the size of $\boldsymbol{\Lambda}$ are determined by the number of sub-ARIS segments K, as described below:

- For $K = 1$: The amplitudes over ARIS elements are assumed to be identical. The beamforming basis and the corresponding positive definite weighting matrix are given by $\mathbf{U} = [\mathbf{a}(\mathbf{p}), \dot{\mathbf{a}}_x(\mathbf{p}), \dot{\mathbf{a}}_y(\mathbf{p})]^* \in \mathbb{C}^{M\times 3}$, and $\boldsymbol{\Lambda} \in \mathbb{C}^{3\times 3}$, respectively. Here, $\dot{\mathbf{a}}_x(\mathbf{p})$ and $\dot{\mathbf{a}}_y(\mathbf{p})$ denote derivative beams that create spatial nulls directed toward location $\mathbf{p}$, thereby enhancing localization and detection capabilities [34], [47].
- For $K > 1$: When K distinct amplitudes are assumed across K virtual sub-ARISs, the beamforming basis is defined as

$$\begin{aligned} \mathbf{U} = [&\mathbf{a}(\mathbf{p}), \dot{\mathbf{a}}_x(\mathbf{p}), \dot{\mathbf{a}}_y(\mathbf{p}), \\ &\dot{\mathbf{a}}_x^{(1)}(\mathbf{p}), \dot{\mathbf{a}}_y^{(1)}(\mathbf{p}), \ldots, \dot{\mathbf{a}}_x^{(K)}(\mathbf{p}), \dot{\mathbf{a}}_y^{(K)}(\mathbf{p})]^*, \end{aligned} \tag{54}$$

where $\mathbf{U} \in \mathbb{C}^{M\times(2K+3)}$ and $\mathbf{\Lambda} \in \mathbb{C}^{(2K+3)\times(2K+3)}$. Each beam $\dot{\mathbf{a}}_x^{(k)}(\mathbf{p})$ and $\dot{\mathbf{a}}_y^{(k)}(\mathbf{p})$ have entries of k-th sub-ARIS, defined as

$$[\dot{\mathbf{a}}_x^{(k)}(\mathbf{p})]_{\left[\frac{M}{K}(k-1)+1:\frac{M}{K}k\right]} = [\dot{\mathbf{a}}_x(\mathbf{p})]_{\left[\frac{M}{K}(k-1)+1:\frac{M}{K}k\right]}, \tag{55}$$

$$[\dot{\mathbf{a}}_y^{(k)}(\mathbf{p})]_{\left[\frac{M}{K}(k-1)+1:\frac{M}{K}k\right]} = [\dot{\mathbf{a}}_y(\mathbf{p})]_{\left[\frac{M}{K}(k-1)+1:\frac{M}{K}k\right]}, \tag{56}$$

with all other entries set to zero.

Proof: See [48, Appendix C] for a detailed derivation of the optimal covariance matrix structure. The formulation in (53) enables the reduction of optimization on the complete covariance matrix $\mathbf{X}$ to the design of a positive semi-definite matrix $\mathbf{\Lambda}$ under a fixed beamforming basis $\mathbf{U}$. In the case of $K > 1$, this construction supports the estimation of K unknowns in $\mathbf{b}$. The inclusion of the derivative beams $\dot{\mathbf{a}}_x^k(\mathbf{p})$ and $\dot{\mathbf{a}}_y^k(\mathbf{p})$ ensures $\mathrm{Rank}\{\mathbf{A}(\mathbf{p})\} = K$, enabling accurate localization across sub-ARIS segments. ■

Proposition 2: With a scaled orthogonalized basis $\mathbf{U}$ such that $\mathbf{U}^H\mathbf{U} = M\mathbf{I}$, the optimization problem can be simplified as

$$\begin{aligned} \min_{\mathbf{\Lambda},\mathbf{u}} \quad & \mathbf{1}^\top \mathbf{u} \\ \text{s.t.} \quad & \begin{bmatrix} \mathbf{J}_K(\boldsymbol{\eta}) & \mathbf{e}_g \\ \mathbf{e}_g & \mathbf{u}_g \end{bmatrix} \succ 0, \quad g = 1, 2, \\ & \mathbf{\Lambda} \succeq 0, \\ & \mathbf{\Lambda} = \mathrm{diag}(\boldsymbol{\lambda}), \quad \boldsymbol{\lambda} \geq 0, \\ & \mathrm{Tr}(\mathbf{\Lambda}) = T. \end{aligned} \tag{57}$$

Proof: See Appendix, for the derivation showing that increasing $\mathrm{Tr}(\mathbf{X})$ leads to a lower PEB. Under the maximum transmit power constraint MT, we orthogonalize $\mathbf{U}$ via the Gram-Schmidt process and normalize such that $\mathbf{U}^H\mathbf{U} = M\mathbf{I}$. This allows us to reformulate the original matrix optimization as a simplified problem over the diagonal matrix $\mathbf{\Lambda}$ in (57). The matrix $\mathbf{U}$ represents the ARIS beamforming configurations, and the entries of $\boldsymbol{\lambda} \in \mathbb{R}^3$ for $K = 1$, or $\boldsymbol{\lambda} \in \mathbb{R}^{2K+3}$ for $K > 1$, can be interpreted as the number of pilots allocated to each corresponding beamforming basis [34], [47]. ■

By following these two propositions, we reduce the original optimization problem from a high-dimensional covariance matrix $\mathbf{X}$ to a low-dimensional diagonal weighting matrix $\mathbf{\Lambda}$. Also, it links the $\mathbf{\Lambda}$ with the pilot number T.

C. Practical Beam Projection

The scaled orthogonal beam matrix $\mathbf{U}$ may contain elements whose power exceeds the unit amplitude constraint, i.e., $|[\mathbf{U}]_{[i,j]}| > 1, \quad \exists(i,j)$. This violates element-wise amplitude limitations imposed by practical ARIS coefficients. Therefore, the beam coefficients in $\mathbf{U}$ must be projected onto a feasible set. The resulting projected matrix is denoted by $\mathbf{W} = [\mathbf{w}_1, \mathbf{w}_2, \ldots, \mathbf{w}_D] \in \mathbb{C}^{M\times D}$, where $D = 3$ when $K = 1$, and $D = 2K + 3$ when $K > 1$. Each column

Algorithm 2 Practical Beam Projection via *constrain, then optimize* Approach

1: Initialize: $\mathbf{U}$
2: **for** $j = 1$ to D **do**
3: $\quad \mathbf{w}_j \leftarrow$ (53)
4: **end for**
5: $\mathbf{W} = [\mathbf{w}_1, \mathbf{w}_2, \ldots, \mathbf{w}_D]$
6: Replace $\mathbf{U}$ with $\mathbf{W}$ in (53)
7: $\mathbf{\Lambda} \leftarrow$ (57)

$\mathbf{w}_j$ is obtained by solving the following convex optimization problem of the form

$$\begin{aligned} \min_{\mathbf{w}_j} \quad & \|[\mathbf{U}]_{[1:T,j]} - \mathbf{w}_j\|^2, \quad \forall j = 1, 2, \ldots, D, \\ \text{s.t.} \quad & |\mathbf{w}_j| \leq \mathbf{1}. \end{aligned} \tag{58}$$

Since the ARIS amplitude constraint $|\mathbf{w}_j| \leq \mathbf{1}$ forms a convex set, the overall problem remains convex. Standard convex solvers, such as CVX [49], can be used to compute the optimal beam set $\mathbf{W}$. Following the "*constrain, then optimize*" strategy from [34], the projected beam vectors $\mathbf{W}$ are used in place of $\mathbf{U}$ in the simplified problem (57) to solve the optimal weighting matrix $\mathbf{\Lambda}$. The detailed procedure is described in Algorithm 2.

Here, $\mathbf{\Lambda}$ indicates weightings of $\mathbf{W}$ over T pilots, and the number is practically an integer. Hence, we round the diagonal entries of $\mathbf{\Lambda}$ to the nearest integer to define the beam appearance duration. It should be noted that each beam in $\mathbf{W}$ must have at least one pilot to prevent an infinite PEB.

D. Codebook Design With Imperfect Knowledge

The above optimization steps rely on the perfect knowledge of $\boldsymbol{\eta}$, which is not necessarily practical. However, $\mathbf{p}$ and ψ can be reasonably approximated using the latest estimated result, e.g., when the UE is tracked by the system. Moreover, $\mathbf{b}$ can be gained by computing the amplitudes corresponding to the centers of sub-ARISs [32], [34]. Assuming the UE is static during a short observation period, the previous estimation output can be used to optimize the codebook for the next estimation stage. Practically, the coarse estimation introduces the uncertainty region $\mathcal{U}$ in the codebook design, and we can generate beams for S potential UE locations which are evenly spaced in the uncertain region and minimize the worst-case PEB through solving (59), conceptually similar to [47]. For $\{\tilde{\boldsymbol{\eta}}_s\}_{s=0}^{S-1}$, we can generate beams $\mathbf{U}(\tilde{\boldsymbol{\eta}}_s)$ and projected beams $\mathbf{W}(\tilde{\boldsymbol{\eta}}_s)$ by solving (58). Then, following the "*constrain, then optimize*" steps to compute the weightings, the optimization problem corresponding to S points can be stated as

$$\begin{aligned} \min_{\mathbf{\Lambda}_s,\mathbf{u}_s} \quad & \mathbf{1}^\top \mathbf{u}_s \\ \text{s.t.} \quad & \begin{bmatrix} \mathbf{J}_K(\tilde{\boldsymbol{\eta}}_s) & \mathbf{e}_g \\ \mathbf{e}_g & \mathbf{u}_{g,s} \end{bmatrix} \succ 0, \quad g = 1, 2, \quad s = 0, 1, \ldots, S, \\ & \mathbf{\Lambda}_s \succeq 0, \\ & \mathbf{\Lambda}_s = \mathrm{diag}(\boldsymbol{\lambda}_s), \\ & \mathrm{Tr}(\mathbf{\Lambda}_s) = T. \end{aligned} \tag{59}$$

The above optimization is solved separately for each candidate parameter vector $\tilde{\boldsymbol{\eta}}_s$, resulting in S independent subproblems

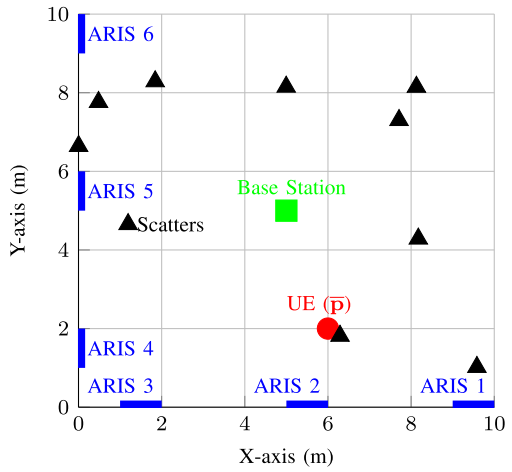

Fig. 2. Top view illustration of the numerical evaluation scenario. Scatterers are marked as black triangles, while green and red markers indicate the locations of the BS and the UE, respectively. The UE position is varied during the evaluations, whereas the locations of the BS, scatterers, and ARIS panels remain fixed unless otherwise noted in text.

in total. Although the optimizations are performed independently, they are linked through a common design goal: to ensure robust codebook performance across the entire uncertainty region $\mathcal{U}$. In practice, one can adopt strategies such as minimizing the worst-case PEB among all s.

E. Complexity of the Codebook Optimization

We solved the problems in (57), (58) and (59) using conventional convex solvers like CVX [49], which typically employ interior-point methods. Computing $\mathbf{\Lambda}$ and $\mathbf{\Lambda}_s$ is independent of M and the beam projection for each instance of the problem scales as $\mathcal{O}(M^3)$ [50]. Since we have D independent beams per point, where D depends on K, the total complexity order for S points is $\mathcal{O}(3SM^3)$ when $K = 1$ and $\mathcal{O}((2K+3)SM^3)$ when $K > 1$.

V. Numerical Results

A. Geometry and Deployment Setup

We consider an example scenario of multiple strip-like ARIS panels equipped on both sides of the walls to form a large ARIS, as shown in Fig. 2. In general, it is sufficient that the ARIS is large only in one dimension with strip-like ARIS allowing for simpler deployments along the room's perimeter [32], while the objective is to estimate the 2D location of the UE. Specifically, each wall has three 1-meter-long physical ARIS panels with $4\,\mathrm{m}$ spacing. Every panel has 188 evenly deployed elements with half-wavelength spacing. Similarly, the other three panels along the y-axis have the same geometry. The locations of the UE and the BS are $\overline{\mathbf{p}} = [6,\, 2,\, 1.8]\ \mathrm{m}$ and $\mathbf{p}_{\mathrm{BS}} = [5,\, 5,\, 2]\ \mathrm{m}$, respectively, as shown in Fig. 2. To evaluate the performance for different user positions, we vary the 2D coordinates $[\overline{x}, \overline{y}]$ of the UE while keeping the height $\overline{z}$ fixed at $1.8\,\mathrm{m}$. Hence, we only refer to 2D coordinates from now on. The geometry of the BS, the scatterers, and ARIS panels remains unchanged throughout the evaluations unless otherwise noted. The codebook $\mathbf{F}$ contains T configurations. Carrier frequency is $28\,\mathrm{GHz}$ and the bandwidth W is $120\,\mathrm{kHz}$.

Since thermal noise power is bandwidth-dependent, a narrowband configuration leads to a relatively low noise power at the receiver. As a result, the transmit power levels used in our evaluations are also modest. Moreover, as the signal-to-noise ratio (SNR) depends on the ARIS configuration through the codebook $\mathbf{F}$, we use and vary systematically the transmit power P_t, ensuring consistency across different evaluation cases.

B. Performance Evaluation With Full-Rank Random Codebook

This subsection evaluates the estimation performance using a full-rank random codebook $\mathbf{F}$ while varying the transmission power P_t from $-20\,\mathrm{dBm}$ to $20\,\mathrm{dBm}$ for a fixed $T = 64$. This transmit power range is selected to show the meaningful accuracy and convergence of BPEB's value in one figure. To evaluate the estimation performance without the impact of the ARIS reflection coefficient's magnitude, we consider an ideal scenario in this subsection where all impinging signals are fully reflected by the ARIS, i.e., $|\omega_{m,t}| = 1$ with random phases. This condition is enforced by the constraint $\mathrm{Tr}(\mathbf{F}\mathbf{F}^H) = MT$.

The RMSE and PEB curves over 300 Monte Carlo realizations for the proposed estimator with $K \in \{2, 6\}$ are shown in Fig. 3. The RMSE($\mathring{\mathbf{p}}$) and RMSE($\overline{\mathbf{p}}$) curves indicate the estimation results regarding the pseudo-true location $\mathring{\mathbf{p}}$ and ground truth location $\overline{\mathbf{p}}$, respectively. For $P_t < -5$ dBm, a noticeable power threshold effect occurs, while the RMSE($\mathring{\mathbf{p}}$) and RMSE($\overline{\mathbf{p}}$) curves for $K = 2$ are closely aligned as the RPB is significantly smaller than those values. Similarly, MPEB and BPEB are close to each other when the transmit power is low. As the transmit power increases, the RMSE($\mathring{\mathbf{p}}$) curve approaches BPEB, while RMSE($\overline{\mathbf{p}}$) aligns with MPEB. According to (45), we know that $\mathrm{BPEB}^2 = \mathrm{MPEB}^2 + \mathrm{RPB}^2$. Thus, when MPEB is small enough, the convergence of BPEB closely approaches RPB, which represents the bias caused by the mismatch between the true and misspecified models. Increasing the number of sub-ARISs to $K = 6$ reduces this mismatch, as evidenced by the reduction in RPB and the convergence of RMSE($\overline{\mathbf{p}}$) shown in Fig. 3(b).

Moreover, the estimated amplitude behavior shown in Fig. 4 indicates that the estimated amplitudes for $K = 6$ align better with the ground truth compared to $K = 2$. However, increasing K introduces more unknowns and increases the variance of individual parameter estimates, as discussed in [51, Sec. 3.7]. Thus, there exists an optimal K under a given transmit power. To analyze the impact of K on the performance, we plot the averaged BPEB curves over 50 realizations of random codebooks in Fig. 5 for two locations. We consider five candidates $\{1, 2, 6, 12, 24\}$ for the assumed K. The random codebook also contains $T = 64$ independent configurations, and they naturally ensure $\mathrm{Rank}\{\mathbf{A}(\mathbf{p})\} = K$, enabling the estimation of K amplitudes when $K < T$. Consequently, the same codebook can be used to evaluate the performance for all cases of K. By fixing $P_t = 0\,\mathrm{dBm}$, we observe that the model misspecification decreases with increasing K, as reflected in

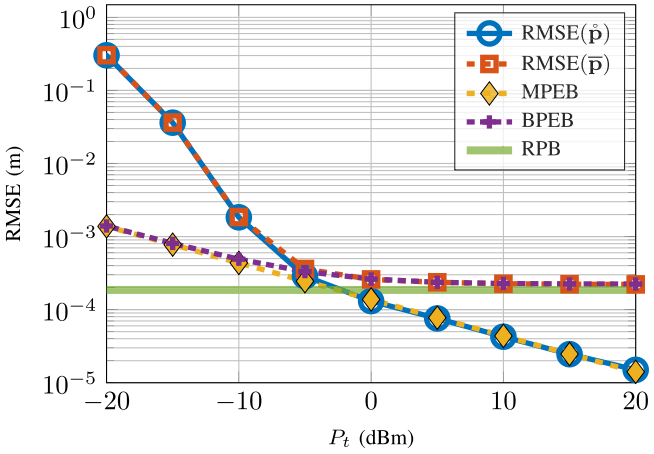

(a) $K = 2$

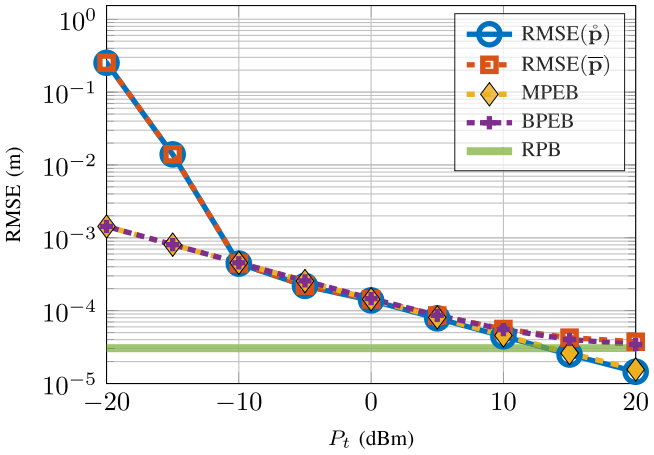

(b) $K = 6$

Fig. 3. Performance evaluation using random codebook. Assumed parameters: $[\overline{x}, \overline{y}] = [6, 2]\,\mathrm{m}$; $T = 64$. The curves shown in the legend correspond to: 1) RMSEs: empirical root-mean-square error of the location estimates, defined in (46). 2) MPEB: misspecified position error bound, defined in (42). 3) BPEB: biased position error bound, defined in (43). 4) RPB: root of position bias, defined in (44).

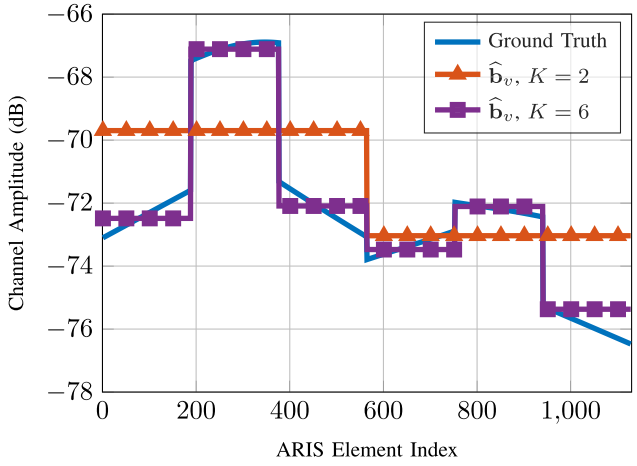

Fig. 4. True element-wise channel amplitudes and estimated channel amplitudes $\widehat{\mathbf{b}}_v$ for $M = 1128$ elements, assuming K sub-ARISs. Assumed parameters: $[\overline{x}, \overline{y}] = [6, 2]\,\mathrm{m}$; $T = 64$; $P_t = 0\,\mathrm{dBm}$; $K \in \{2, 6\}$.

the RPB curves, whereas the BPEB curves show a trend where increasing K initially improves the bound. However, beyond

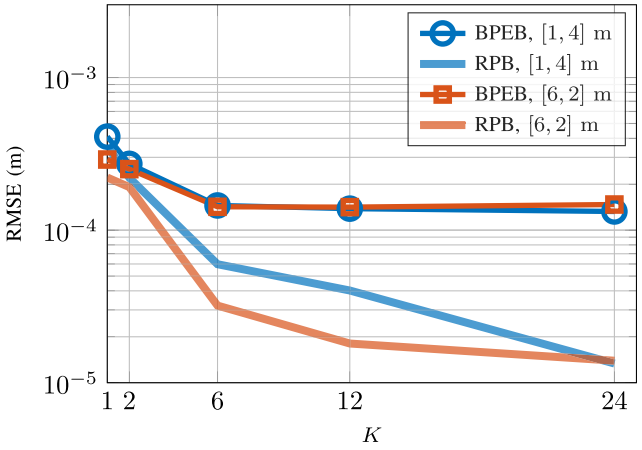

Fig. 5. Average localization BPEB versus K for two different target locations over 50 realizations. Assumed parameters: $[\overline{x}, \overline{y}] = [6, 2]\,\mathrm{m}$ and $[1, 4]\,\mathrm{m}$; $T = 64$; $P_t = 0\,\mathrm{dBm}$.

an optimal point, found at $K = 6$ for the example location of $[6, 2]\,\mathrm{m}$, further increasing the value of K degrades the performance. For another location of $[1, 4]\,\mathrm{m}$, the minimal BPEB is achieved at $K = 24$; however, the curve remains relatively flat beyond $K = 6$, due to the increasing number of unknowns.

In general, although an optimal K exists for a given scenario, it cannot be known exactly a priori due to the unknown mismatch between the true amplitude profile and the assumed piecewise-constant model. However, as discussed in Section III-E, practical guidelines can be used to select a near-optimal K: for instance, by partitioning the ARIS into regions with limited amplitude variation (e.g., within $2-3\,\mathrm{dB}$) based on offline measurements or electromagnetic models, or by evaluating approximate BPEB and residual position bias thresholds using the coarse location estimate $\tilde{\mathbf{p}}$ and prior model knowledge.

C. Performance Evaluation With Perfect Location Knowledge

We next evaluate the estimation performance using the proposed codebook by varying the transmission power P_t from $-40\,\mathrm{dBm}$ to $0\,\mathrm{dBm}$ with $T = 64$. Compared to the previous section, where a random codebook was used, the proposed codebook provides improved performance. Note that, the optimized beam basis obtained from (58) satisfies an element-wise power constraint of at most one. Consequently, the total power constraint for the proposed codebook becomes $\mathrm{Tr}(\mathbf{F}\mathbf{F}^H) \leq MT$. To ensure that the RMSE results remain within a meaningful range, we thus adjusted the transmit power range accordingly, compared to the previous subsection. The results are presented in Fig. 6 for three values of $K \in \{2, 6, 12\}$. For $K = 2$, RMSE($\overline{\mathbf{p}}$) shows a slight decrease and converges to the BPEB, which is relatively large. The reason is that the proposed codebook with $K = 2$ has only 7 independent beam configurations–fewer than $T = 64$ independent configurations of the random codebook–leading thus to increased model misspecification and a larger estimation bias.

Increasing the value of K from 2 to 6 adds diversity to the codebook, reducing estimation bias. For both $K = 6$ and $K = 12$, the curves of RMSE($\mathring{\mathbf{p}}$) and RMSE($\overline{\mathbf{p}}$) closely align,

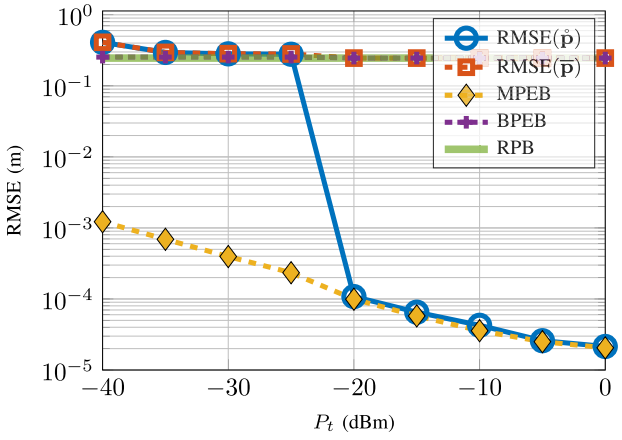

(a) $K = 2$

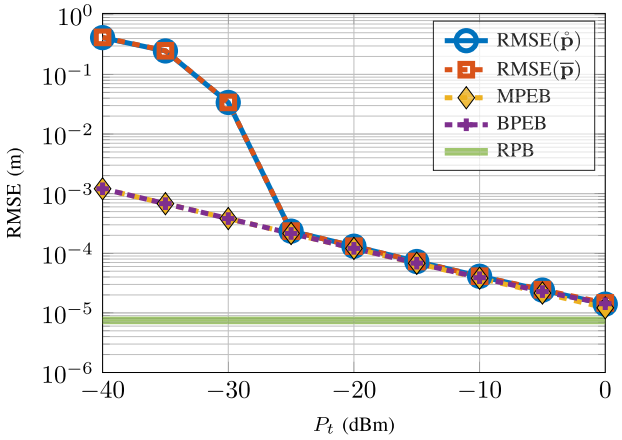

(b) $K = 6$

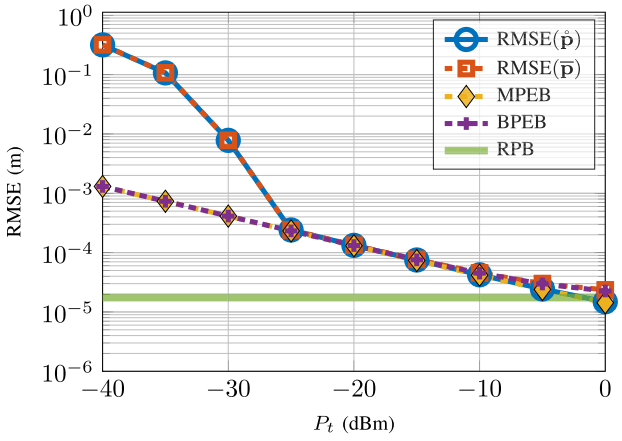

(c) $K = 12$

Fig. 6. Performance evaluation using the proposed codebook. Assumed parameters: $[\overline{x}, \overline{y}] = [6, 2]$ m; $T = 64$; $K \in \{2, 6, 12\}$.

indicating low RPB. Comparing Fig. 3 for the cases of $K = 6$ and $K = 12$, we can find that the proposed codebook in two cases achieves centimeter-level accuracy at $P_t = -30\,\mathrm{dBm}$. Furthermore, one can clearly observe that using the proposed codebook profoundly enhances the performance with lower RMSE and lower bounds.

In general, increasing the value of K reduces model misspecification but also increases parameter variance and alters the structure of the codebook. These three factors jointly affect the localization accuracy. For better visualization, we plot the heat maps of RMSE($\overline{\mathbf{p}}$) for three values of K in Fig. 7, where the UE location $\overline{\mathbf{p}}$ varies in a $9\,\mathrm{m} \times 9\,\mathrm{m}$ square region with a step size of $0.5\,\mathrm{m}$. These heat maps show that increasing K from 2 to 6 leads to a significant performance improvement. Further increasing K to 12 under the same transmit power causes a slight performance reduction for most locations. This shows that increasing K does not always lead to better estimation accuracy in the proposed codebook design. However, determining the optimal K before generating the codebook and performing the estimation is not possible without knowing the true model. Overall, the results show really promising performance when assuming constant amplitudes over 1-meter sub-ARIS ($K = 6$) or 0.5-meter sub-ARIS ($K = 12$) in the considered deployment scenario.

D. Performance With Randomly Drawn Scatterer Locations

Continuing the evaluation of the proposed codebook under perfect UE location knowledge, we next more thoroughly evaluate the impact of scattering-induced multipath on the proposed localization framework. Since the scattering-induced signal $\mathbf{y}_{\mathrm{INT}}$ exists in our evaluations and may also arise in practice, we assess the robustness of the localization performance under varying scattering conditions over 100 independent random realizations for the scatterer locations, drawn from an applicable uniform distribution, while keeping the UE, BS, and ARIS positions the same as in the geometric configuration shown in Fig. 2.

The resulting median RMSE across these realizations, together with corresponding 5th–95th percentiles, are illustrated in Fig. 8 and Fig. 9, respectively. In Fig. 8, the RMSE variations across different scatterer locations are shown for the proposed estimator and the related theoretical bounds as functions of the transmit power P_t. There, the curves indicate the median RMSE values, whereas the shaded areas highlight the 5th–95th percentile regions. As the two RMSE curves are closely aligned at low P_t values, which is as such consistent with all other cases, the corresponding shaded regions overlap. As discussed in Section V-B, the convergence of BPEB and RMSE($\overline{\mathbf{p}}$) aligns with RPB. Then, we can observe that the scatterer-induced RPB variation is more clearly reflected in the shaded region, which represents the 5th–95th percentile ranges of the BPEB and RMSE($\overline{\mathbf{p}}$), when $P_t > -20\,\mathrm{dBm}$. To provide a more clear view of the related variations with the overlapping percentile regions, the results are also illustrated with error bars in Fig. 9 for four separate example values of the transmit power P_t. These results demonstrate that the performance variations across different scatterer deployments are still relatively small, thus indicating robust and meaningful localization performance of the proposed method under various scattering conditions.

E. Performance Under Strong Amplitude Variations Near Walls

In practical indoor deployments, a UE very close to a wall may experience stronger amplitude variations across the ARIS elements, especially within the nearest sub-ARIS region. This

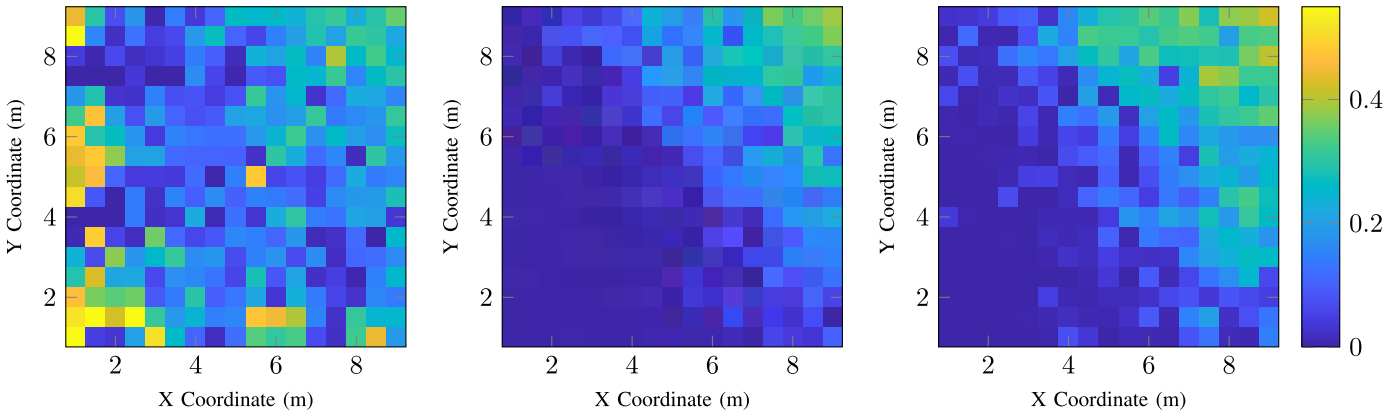

(a) $K = 2$ (b) $K = 6$ (c) $K = 12$

Fig. 7. RMSE heatmaps using the proposed codebook. Assumed parameters: $T = 64$; $P_t = -25\,\text{dBm}$; $K \in \{2, 6, 12\}$.

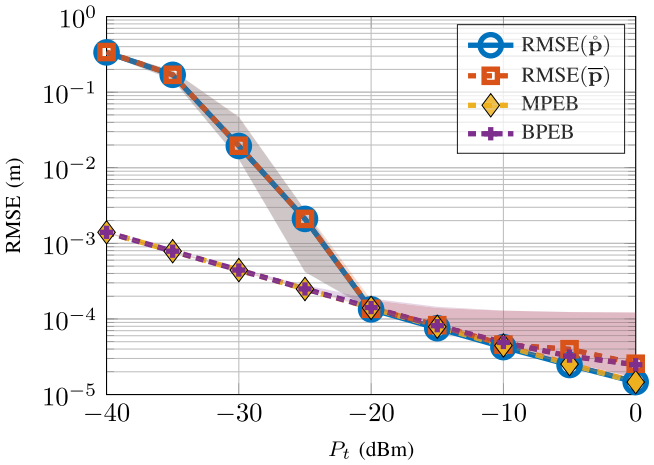

Fig. 8. Median RMSE and corresponding 5th–95th percentile regions across 100 randomly drawn scatterer location realizations as functions of the transmit power P_t. Assumed parameters: $[\overline{x}, \overline{y}] = [6, 2]\,\text{m}$; $T = 64$; $K = 6$.

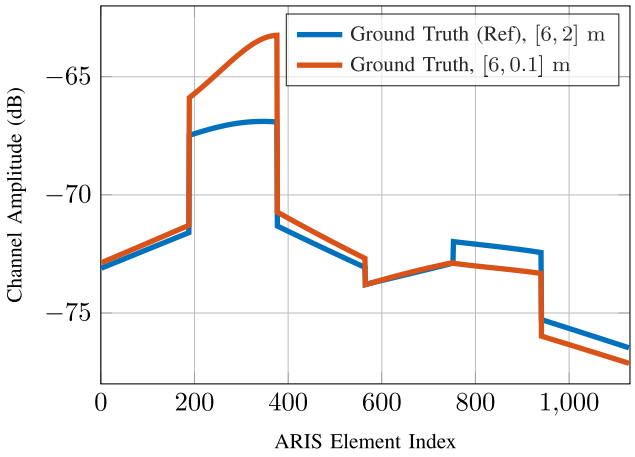

Fig. 10. Illustration of true element-wise channel amplitudes in dB scale for two different UE locations noted in the legend. We can observe more notable variations within an individual sub-ARIS when the UE is located close to the wall (close to one of the physical ARIS panels).

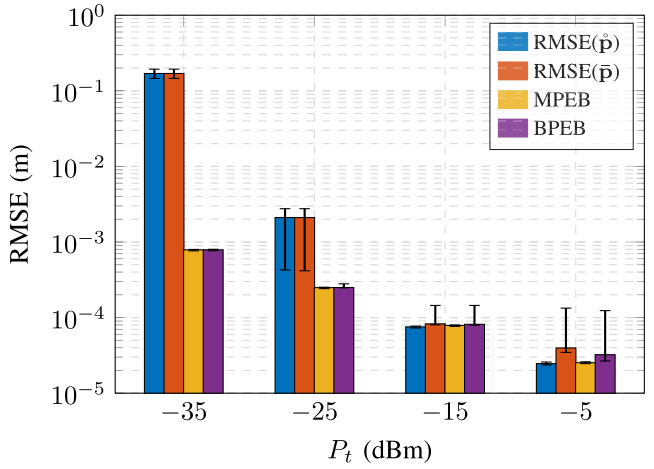

Fig. 9. Median RMSE and corresponding 5th–95th percentile ranges across 100 randomly drawn scatterer location realizations, evaluated at selected transmit power levels of $P_t \in \{-35, -25, -15, -5\}\,\text{dBm}$. Assumed parameters: $[\overline{x}, \overline{y}] = [6, 2]\,\text{m}$; $T = 64$; $K = 6$.

effect is more pronounced when the ARIS is partitioned into a fixed number of virtual sub-ARISs, such as $K = 6$. To examine and also illustrate this, we consider a rather extreme case where the UE is at $[\overline{x}, \overline{y}] = [6, 0.1]$ m, placing it really close to the physical ARIS2 panel. As shown in Fig. 10, the resulting element-wise channel amplitudes show noticeably stronger variation compared to the reference UE location. However, the variations even within the second sub-ARIS panel (element indices 189–376) are still within 3 dB or so, as can be observed through the figure.

Further to the above, Fig. 11 illustrates the UE localization performance achieved using the proposed and random codebooks, respectively, in this extreme scenario. The proposed design uses the perfect UE location information in the codebook optimization. The results demonstrate that both codebooks provide accurate localization; however, the random codebook requires higher transmit power to reach comparable accuracy to the proposed design. Overall, these results highlight the high localization accuracy through the proposed approach, even in such an extreme scenario.

F. Location Uncertainty Evaluation

1) Impact of Location Uncertainty on the Proposed Codebook Approach: Since ARIS codebook optimization relies on

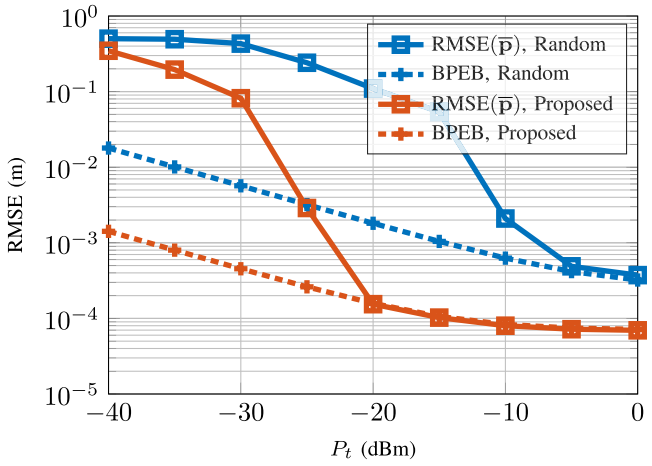

(b) Random Codebook

Fig. 11. Performance evaluation using proposed and random codebooks when the UE is located close to the wall. Assumed parameters: $[\overline{x}, \overline{y}] = [6, 0.1]$ m; $T = 64$; $K = 6$.

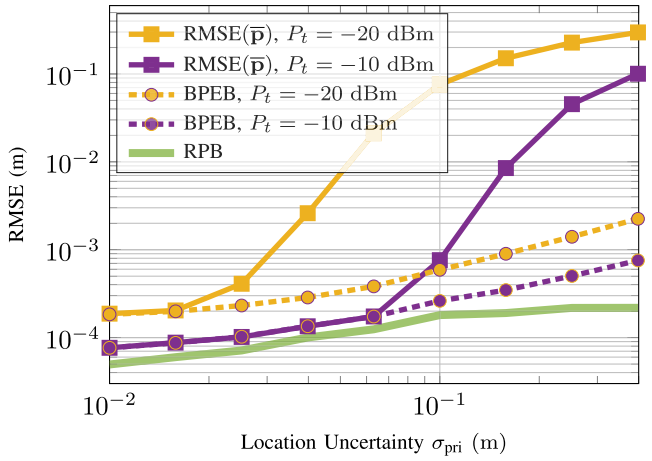

Fig. 12. Performance evaluation using the proposed codebook under prior location uncertainty. Assumed parameters: $[\overline{x}, \overline{y}] = [6, 2]$ m; $T = 64$; $P_t \in \{-20, -10\}$ dBm; $K = 6$.

prior location information, this section first evaluates the effect of location uncertainty on the achievable performance when using beams focusing on the prior location. We assume that the known coarse prior location is given by $\tilde{\mathbf{p}} = \overline{\mathbf{p}} + [\Delta x, \Delta y, 0] \in \mathbb{R}^3$, where Δx and Δy represent the 2D localization bias due to uncertainty. The covariance matrix of the bias is given by $\text{Cov}([\Delta x, \Delta y]^\top [\Delta x, \Delta y]) = \sigma_{\text{pri}}^2 I \in \mathbb{R}^{2\times 2}$, following the definition in [52]. The codebook $\mathbf{F}$ is generated by solving the optimization problem in (57), using $\tilde{\mathbf{p}}$ as the UE location. Figure 12 presents the averaged RMSE and BPEB curves over 50 Monte Carlo trials for $P_t = -20\,\text{dBm}$ and $P_t = -10\,\text{dBm}$. The x-axis shows the location uncertainty, ranging from $0.01\,\text{m}$ to $0.4\,\text{m}$, while the y-axis represents RMSE in meters, ranging from $10^{-4}\,\text{m}$ to $0.6\,\text{m}$. Both axes are plotted on a logarithmic scale. As σ_{pri} increases, the beams in $\mathbf{W}$ steered toward the prior location $\tilde{\mathbf{p}}$ differ from ground truth $\overline{\mathbf{p}}$. These misaligned beams cause some observable performance degradation. For example, we can see the RMSE curve of $P_t = -20\,\text{dBm}$ shifting from the earlier sub-millimeter-level

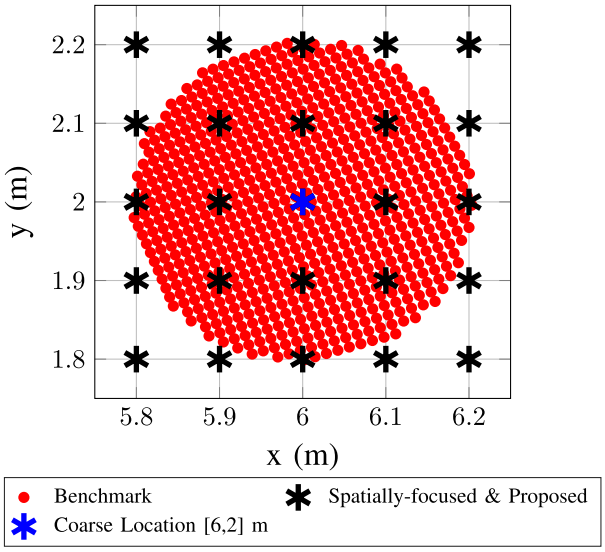

Fig. 13. Example illustration of the beam steering points for the benchmark, spatially-focused, and proposed codebooks. The center location varies with the random seed used for coarse location generation. Assumed parameters: $[\overline{x}, \overline{y}] = [6, 2]$ m, $T = 750$, and $K = 6$.

to decimeter-level accuracy as the uncertainty grows. Besides the increase in the RMSE values with increasing σ_{pri}, the gap between the RMSEs and the corresponding BPEBs also increases, which results from SNR degradation due to beam misalignment. Moreover, the model misspecification increases with increasing uncertainty, as is evident from the RPB curve.

2) Performance Evaluation and Benchmark Comparisons Using Multi-Point Beams: After analyzing the impact of location uncertainty when the beams focus on a single point, we next evaluate the estimation performance using a codebook optimized from (59), which steers beams toward multiple candidate locations to mitigate imperfect prior knowledge. Specifically, we generate $S = 25$ candidate points on a 5×5 grid centered at the coarse prior location $\tilde{\mathbf{p}} = [\tilde{x}, \tilde{y}, \tilde{z}]^\mathsf{T}$, with spacing $d_{\text{grid}} = 0.1\,\text{m}$, expressed as

$$\mathcal{P}_{\text{Prop}} = \Big\{ \tilde{\mathbf{p}}_{n_x,n_y} = \tilde{\mathbf{p}} + [n_x d_{\text{grid}},\, n_y d_{\text{grid}},\, 0]^\mathsf{T} \Big| \, n_x, n_y \in \{-2,-1,0,1,2\} \Big\}. \quad (60)$$

Each candidate point is then indexed as $\tilde{\mathbf{p}}_s$, $s = 1, \ldots, 25$, by a fixed mapping between s and the pairs (n_x, n_y). The coarse location $\tilde{\mathbf{p}}$ is assumed to have a localization error with standard deviation $\sigma_{\text{pri}} = 0.3\,\text{m}$, which reflects typical errors from a low-resolution prior estimation step. The set $\mathcal{P}_{\text{Prop}}$ is then used to design both the *proposed codebook* and the so-called *spatially-focused* codebook, ensuring a fair comparison under equal total transmit power and an equal number of pilot symbols. Solving (59) under this setup yields the proposed codebook for the case with imperfect location knowledge. In contrast, the spatially-focused codebook forms each beam by co-phasing all ARIS elements toward one candidate point $\tilde{\mathbf{p}}_s$, thereby concentrating the reflected signal energy at that location [53]. The resulting 25 steering points are illustrated by the black markers in Fig. 13. Due to the sparsely generated beams for 25 potential points, the resulting spatially-focused codebook achieves a rank higher than the

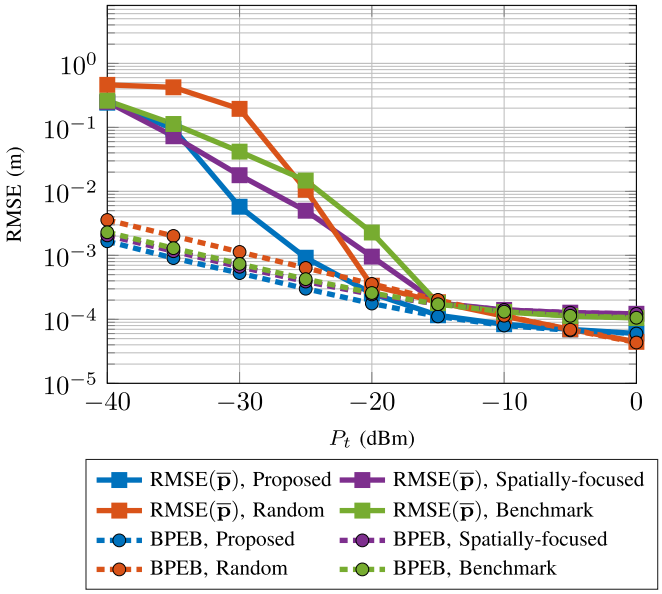

Fig. 14. Average RMSE and BPEB performance using random [32], proposed, spatially-focused [53], and benchmark [54] codebooks under imperfect prior location knowledge. Assumed parameters: $[\overline{x}, \overline{y}] = [6, 2]$ m; $T = 750$; $S = 25$; $K = 6$.

number of unknowns, which enables reliable estimation of the $K = 6$ amplitude parameters of the ARIS. Moreover, in these evaluations, each candidate point is allocated 30 pilot symbols, resulting in a total of $T = 750$ for both the proposed and the spatially-focused codebooks.

For further comparison, we also evaluate the *random codebook* [32] and the *benchmark codebook* from [54] under the same transmit power and pilot limits. The random codebook requires no knowledge of the UE location; it is constructed by setting $|\omega_{m,t}| = 1$ with independently randomized phases across all ARIS elements and time slots, as defined in Section V-B. In contrast, the benchmark codebook relies on the coarse UE location $\tilde{\mathbf{p}}$. Following the methodology in [54], we first generate a dense set of candidate focusing points using the polar-domain sampling procedure described in Algorithm 1, with parameters $N_{\text{BM}} = 1128$ and $\beta_{\text{BM}} = 1.6$. Each sampled angle-distance pair is converted into a Cartesian coordinate, yielding the set $\mathcal{P}_{\text{BM}} = \{\mathbf{p}_{\text{BM},\ell}\}_{\ell=1}^{S_{\text{BM}}}$, where S_{BM} denotes the total number of benchmark points. Given the coarse prior location $\tilde{\mathbf{p}}$, we compute the distance $d_\ell = \|\mathbf{p}_{\text{BM},\ell} - \tilde{\mathbf{p}}\|$ for each point and sort them in ascending order. The T closest benchmark points are then selected as

$$\mathbf{p}_t^{\text{BM}} = \mathbf{p}_{\text{BM},(t)}, \quad t = 1, \ldots, T, \tag{61}$$

where $\mathbf{p}_{\text{BM},(t)}$ denotes the t-th closest point to $\tilde{\mathbf{p}}$. Spatially-focused beam patterns are then formed toward these selected points, as in [54], with the steering locations shown as red markers in Fig. 13.

The corresponding simulation results are shown in Figure 14, which presents the RMSE and BPEB for the random, proposed, spatially-focused, and benchmark codebooks. The true 2D UE location is fixed at $[\overline{x}, \overline{y}] = [6, 2]$ m. Since the generation of the proposed, spatially-focused, and benchmark codebooks depends on the coarse location estimate $\tilde{\mathbf{p}}$, their performance is averaged over 50 Monte Carlo trials on $\tilde{\mathbf{p}}$ to mitigate the effect of outliers.

The obtained RMSE and BPEB results demonstrate that across the transmit power range of $P_t \in [-35, -5]$ dBm, the proposed codebook consistently outperforms the spatially-focused, benchmark, and random codebooks, confirming the effectiveness of the proposed design. At lower transmit powers ($P_t \in [-40, -20]$ dBm), the benchmark codebook performs slightly worse than the spatially-focused one, as also reflected by the corresponding BPEB results. When the transmit power increases to $P_t \in [-15, 0]$ dBm range, both the proposed and the spatially-focused codebooks approach their respective bounds. Although the benchmark codebook benefits from more versatile beam patterns and thus achieves slightly lower BPEB than the spatially-focused design, its overall performance remains worse compared to the proposed approach. For instance, at $P_t = -30$ dBm, the proposed codebook achieves sub-millimeter RMSE accuracy, whereas the random codebook only reaches sub-meter accuracy, with the spatially-focused and benchmark codebooks achieving intermediate performance. As the transmit power further increases ($P_t = -10$ to 0 dBm), the performance gap between the RMSEs and the PEBs narrows down. In this higher-power regime, we observe a slight performance reversal: the full-rank random codebook surpasses the proposed design due to (i) increased RPB for the proposed codebook under larger prior-location uncertainty, leading to beam misalignment, and (ii) the random codebook's full-rank property ($\text{Rank}(\mathbf{F}) = T$), which enhances robustness.

In general, we note that the performance of the proposed codebook approach is dependent on the accuracy of the coarse location prior. Under large location uncertainty, the beams optimized for the inaccurate UE position become misaligned with the true location. This misalignment degrades the performance of BPEB and RPB. The rise in RPB limits performance convergence; hence, we observe that the random codebook eventually outperforms the designed codebook at the highest transmit powers. However, and importantly, we also wish to note that the proposed codebook approach largely outperforms the random codebook reference method for a wide range of TX powers that correspond to meaningful received SNRs.

VI. Conclusion

This work investigated the adoption and optimization of absorptive RIS panels for near-field UE localization under channel spatial non-stationarity and model misspecification. To manage the complexity arising from estimating the element-wise channel amplitudes, we introduced a virtual sub-region or sub-ARIS based misspecified model that significantly reduces the number of unknown parameters compared to full-fledged near-field models that incorporate channel SNS across all elements, thereby simplifying the estimation task. Building on this, we developed a low-complexity MML estimator with closed-form solutions for acquiring estimates of position, phase, and amplitudes. We further provided a theoretical performance analysis framework using the MCRB approach, quantifying the performance degradation due to model misspecification, while also allowing to propose and

establish practical sub-ARIS selection rules based on BPEB and RPB thresholds. A vast set of empirical numerical results demonstrated that the proposed reduced-complexity localization algorithm approaches the theoretical performance bounds.

Moreover, we proposed a codebook optimization framework based on the developed models to further enhance the localization accuracy. The provided empirical results validated the efficiency of the proposed codebook optimization algorithm, demonstrating near-bound performance even with low transmit powers and meaningful robustness against the multipath impacts. While the proposed codebook optimization approach was generally shown to outperform all three reference codebooks, minor mutual performance deviations were observed under extreme conditions, when the pilot number, transmit power, and location uncertainty are all high, where the full-rank random codebook can outperform the proposed one, highlighting a potential robustness issue under severe prior uncertainties.

In general, hardware imperfections related effects–including mutual coupling, energy leakage, amplitude/phase quantization, and frequency-dependent responses–can also be viewed as sources of model misspecification, and are therefore natural extensions of the present framework. Our future work will build on these findings by addressing such hardware-induced mismatches while also incorporating Doppler effects in mobile scenarios, as well as exploring wideband multicarrier systems and their associated near-field signal structures.

APPENDIX
RELATIONSHIP BETWEEN PEB AND $\mathrm{Tr}(\mathbf{X})$

To prove the relationship between PEB and $\mathrm{Tr}(\mathbf{X})$, we suppose an initial covariance matrix $\mathbf{X}_0$ satisfying $\mathrm{Tr}(\mathbf{X}) \leq MT$. Then we scale the covariance matrix as follows

$$\mathbf{X}(\alpha) = \alpha \mathbf{X}_0, \quad \alpha > 0. \tag{62}$$

Consequently, the scaled covariance trace becomes

$$\mathrm{Tr}(\mathbf{X}(\alpha)) = \alpha \,\mathrm{Tr}(\mathbf{X}_0), \tag{63}$$

which leads directly to a linear scaling of the FIM as

$$\mathbf{J}_K(\boldsymbol{\eta}, \mathbf{X}(\alpha)) = \alpha \,\mathbf{J}_K(\boldsymbol{\eta}, \mathbf{X}_0). \tag{64}$$

Thus, the PEB scales explicitly as

$$\mathrm{PEB}(\mathbf{X}(\alpha)) = \sqrt{\frac{1}{\alpha}\mathrm{Tr}\left([\mathbf{J}_K^{-1}(\boldsymbol{\eta}, \mathbf{X}_0)]_{1:2,1:2}\right)} = \frac{1}{\sqrt{\alpha}}\mathrm{PEB}(\mathbf{X}_0). \tag{65}$$

Clearly, we can find that a larger $\mathrm{Tr}(\mathbf{X})$ leads to a lower PEB.

REFERENCES

[1] N. González-Prelcic et al., "The integrated sensing and communication revolution for 6G: Vision, techniques, and applications," *Proc. IEEE*, vol. 112, no. 7, pp. 676–723, Jul. 2024.

[2] J. Tang, M. Cui, S. Xu, L. Dai, F. Yang, and M. Li, "Transmissive RIS for B5G communications: Design, prototyping, and experimental demonstrations," *IEEE Trans. Commun.*, vol. 71, no. 11, pp. 6605–6615, Nov. 2023.

[3] Q. Zhu, M. Li, R. Liu, and Q. Liu, "Joint transceiver beamforming and reflecting design for active RIS-aided ISAC systems," *IEEE Trans. Veh. Technol.*, vol. 72, no. 7, pp. 9636–9640, Jul. 2023.

[4] M. Ahmed et al., "A survey on STAR-RIS: Use cases, recent advances, and future research challenges," *IEEE Internet Things J.*, vol. 10, no. 16, pp. 14689–14711, Aug. 2023.

[5] J. Wang, W. Tang, S. Jin, C.-K. Wen, X. Li, and X. Hou, "Hierarchical codebook-based beam training for RIS-assisted mmWave communication systems," *IEEE Trans. Commun.*, vol. 71, no. 6, pp. 3650–3662, Jun. 2023.

[6] Z. Zhang, T. Jiang, and W. Yu, "Localization with reconfigurable intelligent surface: An active sensing approach," *IEEE Trans. Wireless Commun.*, vol. 23, no. 7, pp. 7698–7711, Jul. 2024.

[7] A. Umer, I. Müürsepp, M. M. Alam, and H. Wymeersch, "Reconfigurable intelligent surfaces in 6G radio localization: A survey of recent developments, opportunities, and challenges," *IEEE Commun. Surveys Tuts.*, vol. 27, no. 6, pp. 3526–3560, Dec. 2025.

[8] E. Basar, M. Di Renzo, J. De Rosny, M. Debbah, M.-S. Alouini, and R. Zhang, "Wireless communications through reconfigurable intelligent surfaces," *IEEE Access*, vol. 7, pp. 116753–116773, 2019.

[9] X. Mu, Y. Liu, L. Guo, J. Lin, and R. Schober, "Simultaneously transmitting and reflecting (STAR) RIS aided wireless communications," *IEEE Trans. Wireless Commun.*, vol. 21, no. 5, pp. 3083–3098, May 2022.

[10] J. Xu, X. Mu, J. T. Zhou, and Y. Liu, "Simultaneously transmitting and reflecting (STAR)-RISs: Are they applicable to dual-sided incidence?" *IEEE Wireless Commun. Lett.*, vol. 12, no. 1, pp. 129–133, Jan. 2023.

[11] R. Fara, P. Ratajczak, D.-T. Phan-Huy, A. Ourir, M. Di Renzo, and J. de Rosny, "A prototype of reconfigurable intelligent surface with continuous control of the reflection phase," *IEEE Wireless Commun.*, vol. 29, no. 1, pp. 70–77, Feb. 2022.

[12] M. Rahal et al., "Performance of RIS-aided near-field localization under beams approximation from real hardware characterization," *EURASIP J. Wireless Commun. Netw.*, vol. 2023, no. 1, p. 86, Aug. 2023.

[13] F. Wang and A. L. Swindlehurst, "Applications of absorptive reconfigurable intelligent surfaces in interference mitigation and physical layer security," *IEEE Trans. Wireless Commun.*, vol. 23, no. 5, pp. 3918–3931, May 2024.

[14] Z. Lin et al., "Self-powered absorptive reconfigurable intelligent surfaces for securing satellite-terrestrial integrated networks," *China Commun.*, vol. 21, no. 9, pp. 276–291, Sep. 2024.

[15] Q. Hu, H. Yang, X. Zeng, Y. Rao, and X. Y. Zhang, "Methodology and design of absorptive filtering reconfigurable intelligent surfaces," *IEEE Trans. Antennas Propag.*, vol. 72, no. 6, pp. 5301–5306, Jun. 2024.

[16] A. Tabeshnezhad, Y. Zhu, A. Vilenskiy, V. Ly Nguyen, A. Lee Swindlehurst, and T. Svensson, "Jammer mitigation in absorptive RIS-assisted uplink NOMA," 2024, *arXiv:2408.16786*.

[17] K. Keykhosravi et al., "Leveraging RIS-enabled smart signal propagation for solving infeasible localization problems: Scenarios, key research directions, and open challenges," *IEEE Veh. Technol. Mag.*, vol. 18, no. 2, pp. 20–28, Jun. 2023.

[18] H. Zhang, H. Zhang, B. Di, K. Bian, Z. Han, and L. Song, "MetaLocalization: Reconfigurable intelligent surface aided multi-user wireless indoor localization," *IEEE Trans. Wireless Commun.*, vol. 20, no. 12, pp. 7743–7757, Dec. 2021.

[19] H. Kim et al., "RIS-aided monostatic sensing and object detection with single and double bounce multipath," in *Proc. IEEE Int. Conf. Commun. Workshops (ICC Workshops)*, May 2023, pp. 1883–1889.

[20] Z. Xing, R. Wang, and X. Yuan, "An efficient solution to phase-shift optimization for RIS enabled joint communication and sensing," *IEEE Trans. Veh. Technol.*, vol. 73, no. 12, pp. 19901–19906, Dec. 2024.

[21] J. Zhang, J. Wu, and R. Wang, "User localization and environment mapping with the assistance of RIS," *IEEE Trans. Veh. Technol.*, vol. 73, no. 6, pp. 8549–8562, Jun. 2024.

[22] A. Elzanaty, A. Guerra, F. Guidi, and M.-S. Alouini, "Reconfigurable intelligent surfaces for localization: Position and orientation error bounds," *IEEE Trans. Signal Process.*, vol. 69, pp. 5386–5402, 2021.

[23] Z. Ebadi, A. M. Molaei, M. A. B. Abbasi, S. Cotton, A. Tukmanov, and O. Yurduseven, "Electromagnetic informed data model considerations for near-field DOA and range estimates," *Sci. Rep.*, vol. 14, no. 1, p. 15271, Jul. 2024.

[24] A. Fadakar, M. F. Keskin, H. Chen, H. Wymeersch, and A. F. Molisch, "Near-field RIS-assisted localization under mutual coupling," in *Proc. IEEE Int. Conf. Commun. Workshops (ICC Workshops)*, Jun. 2025, pp. 1470–1475.

[25] E. Björnson, H. Wymeersch, B. Matthiesen, P. Popovski, L. Sanguinetti, and E. de Carvalho, "Reconfigurable intelligent surfaces: A signal processing perspective with wireless applications," *IEEE Signal Process. Mag.*, vol. 39, no. 2, pp. 135–158, Mar. 2022.

[26] Z. Wang, Z. Liu, Y. Shen, A. Conti, and M. Z. Win, "Holographic localization with synthetic reconfigurable intelligent surfaces," *IEEE J. Sel. Topics Signal Process.*, vol. 18, no. 4, pp. 603–618, May 2024.
[27] M. Rahal, A. Elzanaty, M. Mirmohseni, Y. Ma, and R. Tafazolli, "Near-field wideband ISAC: Estimator design and performance analysis," *IEEE Trans. Aerosp. Electron. Syst.*, early access, Sep. 3, 2025, doi: 10.1109/TAES.2025.3605909.
[28] Z. Ebadi, A. M. Molaei, M. A. B. Abbasi, S. L. Cotton, A. Tukmanov, and O. Yurduseven, "Near-field source localization and velocity estimation using an extremely large antenna array," in *Proc. IEEE 26th Int. Workshop Signal Process. Artif. Intell. Wireless Commun. (SPAWC)*, Sep. 2025, pp. 1–5.
[29] A. Guerra, F. Guidi, D. Dardari, and P. M. Djuric, "Near-field tracking with large antenna arrays: Fundamental limits and practical algorithms," *IEEE Trans. Signal Process.*, vol. 69, pp. 5723–5738, 2021.
[30] S. Huang, B. Wang, Y. Zhao, and M. Luan, "Near-field RSS-based localization algorithms using reconfigurable intelligent surface," *IEEE Sensors J.*, vol. 22, no. 4, pp. 3493–3505, Feb. 2022.
[31] Y. Pan, C. Pan, S. Jin, and J. Wang, "RIS-aided near-field localization and channel estimation for the terahertz system," *IEEE J. Sel. Topics Signal Process.*, vol. 17, no. 4, pp. 878–892, Jul. 2023.
[32] D. Dardari, N. Decarli, A. Guerra, and F. Guidi, "LOS/NLOS near-field localization with a large reconfigurable intelligent surface," *IEEE Trans. Wireless Commun.*, vol. 21, no. 6, pp. 4282–4294, Jun. 2022.
[33] Z. Abu-Shaban, K. Keykhosravi, M. F. Keskin, G. C. Alexandropoulos, G. Seco-Granados, and H. Wymeersch, "Near-field localization with a reconfigurable intelligent surface acting as lens," in *Proc. ICC - IEEE Int. Conf. Commun.*, Jun. 2021, pp. 1–6.
[34] M. Rahal, B. Denis, K. Keykhosravi, M. F. Keskin, B. Uguen, and H. Wymeersch, "Constrained RIS phase profile optimization and time sharing for near-field localization," in *Proc. IEEE 95th Veh. Technol. Conf. (VTC-Spring)*, Jun. 2022, pp. 1–6.
[35] H. Zhang et al., "Reconfigurable intelligent surface-assisted localization in OFDM systems with carrier frequency offset and phase noise," 2023, *arXiv:2312.12534*.
[36] C. Ozturk, M. F. Keskin, H. Wymeersch, and S. Gezici, "RIS-aided near-field localization under phase-dependent amplitude variations," *IEEE Trans. Wireless Commun.*, vol. 22, no. 8, pp. 5550–5566, Aug. 2023.
[37] B. Sun et al., "Near-field RIS-aided localization under channel non-stationarity: A mismatched model approach," in *Proc. IEEE 25th Int. Workshop Signal Process. Adv. Wireless Commun. (SPAWC)*, Jul. 2024, pp. 271–275.
[38] A. M. Kuzminskiy, A. Elzanaty, G. Gradoni, F. Wang, and R. Tafazolli, "Near-field localization with physics-compliant electromagnetic model: Algorithms and model mismatch analysis," *IEEE Internet Things J.*, vol. 12, no. 15, pp. 30533–30547, Aug. 2025.
[39] Ö. Özdogan, E. Björnson, and E. G. Larsson, "Intelligent reflecting surfaces: Physics, propagation, and pathloss modeling," *IEEE Wireless Commun. Lett.*, vol. 9, no. 5, pp. 581–585, May 2020.
[40] K. Keykhosravi and H. Wymeersch, "Multi-RIS discrete-phase encoding for interpath-interference-free channel estimation," 2021, *arXiv:2106.07065*.
[41] T. Ma, Y. Xiao, X. Lei, W. Xiong, and M. Xiao, "Spreading CDMA via RIS: Multipath separation, estimation, and combination," *IEEE Internet Things J.*, vol. 10, no. 13, pp. 11396–11413, Jul. 2023.
[42] S. Fortunati, F. Gini, M. S. Greco, and C. D. Richmond, "Performance bounds for parameter estimation under misspecified models: Fundamental findings and applications," *IEEE Signal Process. Mag.*, vol. 34, no. 6, pp. 142–157, Nov. 2017.
[43] H. L. V. Trees, *Detection, Estimation, and Modulation Theory, Part I*. Hoboken, NJ, USA: Wiley, 2001.
[44] H. Lu and Y. Zeng, "Communicating with extremely large-scale Array/surface: Unified modeling and performance analysis," *IEEE Trans. Wireless Commun.*, vol. 21, no. 6, pp. 4039–4053, Jun. 2022.
[45] J. Xu, X. Mu, and Y. Liu, "Exploiting STAR-RISs in near-field communications," *IEEE Trans. Wireless Commun.*, vol. 23, no. 3, pp. 2181–2196, Mar. 2024.
[46] S. Boyd and L. Vandenberghe, *Convex Optimization*. Cambridge, U.K.: Cambridge Univ. Press, 2004, ch. vol. 7, pp. 400–402.
[47] M. F. Keskin, F. Jiang, F. Munier, G. Seco-Granados, and H. Wymeersch, "Optimal spatial signal design for mmWave positioning under imperfect synchronization," *IEEE Trans. Veh. Technol.*, vol. 71, no. 5, pp. 5558–5563, May 2022.
[48] J. Li, L. Xu, P. Stoica, K. W. Forsythe, and D. W. Bliss, "Range compression and waveform optimization for MIMO radar: A Cramér–Rao bound based study," *IEEE Trans. Signal Process.*, vol. 56, no. 1, pp. 218–232, Jan. 2008.
[49] M. Grant and S. Boyd, "Graph implementations for nonsmooth convex programs," in *Recent Advances in Learning and Control*, vol. 371. Cham, Switzerland: Springer, 2008, pp. 95–110.
[50] S. Boyd and L. Vandenberghe. (2023). *Convex Optimization*. [Online]. Available: https://stanford.edu/ boyd/cvxbook/bv_cvxslides.pdf
[51] S. M. Kay, *Fundamentals of Statistical Signal Processing: Estimation Theory*, vol. 1. Englewood Cliffs, NJ, USA: Prentice-Hall, 1993.
[52] H. Chen, P. Zheng, M. F. Keskin, T. Al-Naffouri, and H. Wymeersch, "Multi-RIS-enabled 3D sidelink positioning," *IEEE Trans. Wireless Commun.*, vol. 23, no. 8, pp. 8700–8716, Aug. 2024.
[53] S. Droulias, G. Stratidakis, and A. Alexiou, "Near-field engineering in RIS-aided links: Beamfocusing analytical performance assessment," *IEEE Access*, vol. 12, pp. 29536–29546, 2024.
[54] M. Cui and L. Dai, "Channel estimation for extremely large-scale MIMO: Far-field or near-field?" *IEEE Trans. Commun.*, vol. 70, no. 4, pp. 2663–2677, Apr. 2022.

Bo Sun (Member, IEEE) received the Master of Science degree in the field of wireless communications and radio frequency systems from Tampere University, Tampere, Finland, in 2019, where he is currently pursuing the Doctor of Science (Tech.) degree with the Faculty of Information Technology and Communication Sciences. His research interests include 5G and 6G communication systems, OFDM, radar systems, and reconfigurable intelligent surfaces.

Musa Furkan Keskin (Member, IEEE) received the Ph.D. degree in electrical and electronics engineering from Bilkent University, Ankara, Türkiye, in 2018. He is currently a Research Specialist with the Department of Electrical Engineering, Chalmers University of Technology, Gothenburg, Sweden, where he is leading and contributing to various interdisciplinary and industry-focused research projects at both Swedish and European levels, with a specialization in integrated localization, communication, and sensing in 6G systems. His awards include the EU MSCA Postdoctoral Fellowship for the project "OTFS-RADCOM: A New Waveform for Joint Radar and Communications Beyond 5G" and Swedish Research Council (VR) Starting Grant for the Project "Localization and Sensing for Perceptive Cell-Free Networks Towards 6G." He serves as an Editor for IEEE TRANSACTIONS ON COMMUNICATIONS and IEEE TRANSACTIONS ON MOBILE COMPUTING.

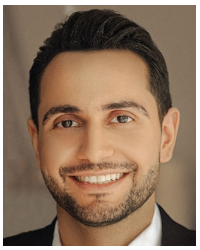

Alireza Pourafzal (Member, IEEE) received the bachelor's degree in electrical engineering and the master's degree in wireless communications from the K. N. Toosi University of Technology, Iran, in 2016 and 2019, respectively, and the Ph.D. degree in information and communication technology from Norwegian University of Science and Technology (NTNU) in 2023. He is currently a Post-Doctoral Researcher with the Communication Group, Chalmers University of Technology, Sweden. His research interests include array signal processing, channel estimation, DOA estimation, and machine learning for wireless and optical communications.

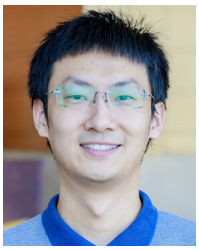

Hui Chen (Member, IEEE) received the Ph.D. degree in electrical and computer engineering from the King Abdullah University of Science and Technology, Saudi Arabia, in 2021. He is currently a Research Specialist with the Chalmers University of Technology, Sweden. Prior to this, he was a Post-Doctoral Researcher with the Chalmers University of Technology from 2021 to 2023 and a Senior Researcher with the Technology Innovation Institute, United Arab Emirates, from 2023 to 2024. His current research interests include 5G/6G radio localization and distributed ISAC.

Moustafa Rahal received the Ph.D. degree in telecommunications engineering from IETR, University of Rennes 1, Rennes, France. During his thesis studies, he was part of the Wireless Technologies Department, CEA-Leti, Grenoble, France, and was fully involved in the EU H2020 RISE-6G Project, during which he was a Visiting Researcher at the Chalmers University of Technology, Gothenburg, Sweden. From December 2023 to February 2025, he was a Post-Doctoral Researcher at the Institute for Communication Systems (ICS), Home of the 5G/6G Innovation Center, University of Surrey, Guildford, U.K. Since January 2025, he has been with Vicinity Technologies Ltd. His research interests include integrating communication and sensing functionalities in near-field scenarios, with a focus on RIS-aided localization in near-field environments for 6G systems.

Jukka Talvitie (Member, IEEE) received the M.Sc. and D.Sc. degrees from Tampere University of Technology, Finland, in 2008 and 2016, respectively. He is currently a University Lecturer with the Unit of Electrical Engineering, Tampere University (TAU), Finland. His research interests include signal processing for wireless communications, radio-based positioning and sensing, radio link waveform design, and radio system design, particularly concerning 5G and beyond mobile technologies.

Henk Wymeersch (Fellow, IEEE) received the Ph.D. degree in electrical engineering/applied sciences from Ghent University, Belgium, in 2005. He is currently a Professor of communication systems with the Department of Electrical Engineering, Chalmers University of Technology, Sweden, and a Distinguished Visiting Professor at Tsinghua University. Prior to joining the Chalmers University of Technology, he was a Post-Doctoral Researcher with the Laboratory for Information and Decision Systems, Massachusetts Institute of Technology, from 2005 to 2009. His current research interests include the convergence of communication and sensing in a 5G and Beyond 5G context. He served as an Associate Editor for IEEE COMMUNICATION LETTERS, IEEE TRANSACTIONS ON WIRELESS COMMUNICATIONS, and IEEE TRANSACTIONS ON COMMUNICATIONS. From 2019 to 2021, he was an IEEE Distinguished Lecturer with the Vehicular Technology Society. He is a Senior Editorial Board Member of *IEEE Signal Processing Magazine*.

Mikko Valkama (Fellow, IEEE) received the M.Sc. (Tech.) and D.Sc. (Tech.) degrees (Hons.) from Tampere University of Technology, Finland, in 2000 and 2001, respectively. In 2003, he was with the Communications Systems and Signal Processing Institute, SDSU, San Diego, CA, USA, as a Visiting Research Fellow. Currently, he is a Full Professor and the Head of the Unit of Electrical Engineering, Tampere University, Finland. His research interests include radio communications, radio localization, and radio-based sensing, with a particular current emphasis on 5G and 6G mobile radio networks.